Timescales of outlet-glacier flow with negligible basal friction: Theory, observations and modeling

Johannes Feldmann[1] and Anders Levermann[1,2,3]

[1]Potsdam Institute for Climate Impact Research (PIK), Potsdam, Germany
[2]Department of Geography and Environmental Sciences, Northumbria University, Newcastle, UK
[3]Institute of Physics, University of Potsdam, Potsdam, Germany

Correspondence: Johannes Feldmann (johannes.feldmann@pik-potsdam) & Anders Levermann
(anders.levermann@pik-potsdam.de)

Abstract. The timescales of the flow and retreat of Greenland's and Antarctica's outlet glaciers and their potential instabilities are arguably the largest uncertainty in future sea-level projections. Here we derive a scaling relation that allows the comparison of the timescales of observed complex ice flow fields with geometric similarity. The scaling relation is derived under the assumption of fast, laterally confined, geometrically similar outlet-glacier flow over a slippery bed, i.e., with negligible basal

5 friction. According to the relation, the time scaling of the outlet flow is determined by the product of the inverse of 1) the fourth power of the width-to-length ratio of its confinement, 2) the third power of the confinement depth and 3) the temperature-dependent ice softness. For the outflow at the grounding line of streams with negligible basal friction this means that the volume flux is proportional to the ice temperature and the bed depth, but goes with the fourth power of the gradient of the bed and with the fifth power of the width of the stream. We show that the theoretically derived scaling relation is supported by

10 the observed velocity scaling of outlet glaciers across Greenland as well as by idealized numerical simulations of marine ice-sheet instabilities (MISIs) as found in Antarctica. Assuming a proportionality between the flow itself and its spatial derivative, we combine the scaling relation with a statistical analysis of the topography of 13 MISI-prone Antarctic outlets. Under these assumptions the timescales in response to a potential destabilization are fastest for Thwaites Glacier in West Antarctica and Mellor, Ninnis and Cook Glaciers in East Antarctica; between 16 and 67 times faster than for Pine Island Glacier. While

15 the applicability of our results is limited by several strong assumptions, the utilization and potential further development of the presented scaling approach may help to constrain time-scale estimates of outlet glacier-flow, augmenting the commonly exploited and comparatively computationally expensive approach of numerical modeling.

1 Introduction

Global sea-level rise is increasingly driven by the contributions of the ice sheets of Greenland and Antarctica. Both ice sheets
20 are observed to be out of balance (The IMBIE team, 2018; Rignot et al., 2019; Mouginot et al., 2019; The IMBIE Team, 2020; Diener et al., 2021). This imbalance is mainly due to the increased discharge of ice into the ocean which accounts for more than half of the cumulative net mass loss from the Greenland Ice Sheet and virtually all of the loss from the Antarctic Ice Sheet. Their discharge is projected to raise global sea level by several decimeters within the 21st century (Bamber et al.,

2019; Levermann et al., 2020; Pattyn and Morlighem, 2020; Edwards et al., 2021; DeConto et al., 2021). Fed by snowfall,
25 the ice sheets spread under their own weight towards the ocean. The flow of the ice accelerates from the interior to the coast,
where the ice sheets are drained by numerous outlet glaciers that often stream through topographic confinements, e.g., valley-
shaped bed troughs, before they discharge into the ocean (Morlighem et al., 2017; Maier et al., 2019; Morlighem et al., 2020).
Such confinements tend to induce stabilizing ice-internal stresses that are transmitted upstream, exerting a buttressing effect on
the hinterland (MacAyeal, 1989; Dupont and Alley, 2005; Schoof, 2007; Gudmundsson et al., 2012; Haseloff and Sergienko,
30 2018; Pegler, 2018), regulating the flow speed and thus the rate of ice discharge into the ocean. Note that we refer to the
term "buttressing" as a backforce induced by laterally confined ice flow that is either floating (often referred to as "ice-shelf
buttressing") or grounded.

In both ice sheets large portions of the observed ice discharge occur due to complex ice geometry in the fast flowing outlet
glaciers of, e.g., Jakobshavn, Helheim or Kangerlussuaq Glaciers in Greenland (Catania et al., 2020; The IMBIE Team, 2020)
35 and Pine Island or Thwaites Glaciers in West Antarctica (Mouginot et al., 2014; The IMBIE team, 2018; Diener et al., 2021).
In Antarctica large parts of the ice is grounded below sea level with a bed topography that is sloping down in landward
direction (retrograde slope; Pattyn and Morlighem, 2020; Morlighem et al., 2020). These two pre-conditions make the ice
sheet prone to the so-called marine ice sheet instability (MISI), a positive feedback between ice discharge and ice-sheet retreat
down the retrograde bed slope (Weertman, 1974; Schoof, 2007; Pattyn and Morlighem, 2020). The buttressing effect of laterally
40 confined ice flow can slow down or even prevent MISI-type destabilization (Gudmundsson et al., 2012; Haseloff and Sergienko,
2018; Pegler, 2018). The development of a MISI was hypothesized for the West Antarctic Ice Sheet more than forty years ago
(Hughes, 1973; Mercer, 1978) and meanwhile could indeed have been initiated as suggested by observations and ice-dynamical
modeling (Favier et al., 2014; Joughin et al., 2014; Seroussi et al., 2017; The IMBIE Team, 2020; Diener et al., 2021).

The quantitative influence of buttressing on the timescales of confined ice flow and the related discharge in general as well
45 as on MISI timescales in particular require detailed numerical computations (Favier et al., 2014; Joughin et al., 2014; Pattyn
and Morlighem, 2020). By comparing similar ice dynamics it is however possible to derive scaling relations that comprise the
complex stress and velocity field without the need of computationally expensive simulations (Feldmann and Levermann, 2016;
Levermann and Feldmann, 2019). Such relations provide a link between the characteristic scales of a glacier, e.g., between its
ice-flow timescale and its geometric dimensions. While scaling relations are valid for each glacier separately they also allow the
50 comparison of similar glaciers, e.g., the comparison between the timescales of two glaciers based on their individual geometric
scales.

To derive the scaling relation presented here, we conduct a scaling analysis of the governing dynamic equations of fast,
shallow and laterally confined ice flow under the assumption of small basal friction. To this end, we employ the concept
of similitude (Rayleigh, 1915), which is a common and simple procedure in hydrodynamics and engineering to investigate
55 the scaling behavior of physical systems (Szücs, 1980). A famous example for its application is the Reynolds' number for
the Navier-Stokes equation (Reynolds, 1883; Kundu et al., 2012). A fixed Reynolds's number provides a scaling relation that

ensures similar flow patterns of a fluid under variation of its characteristic properties. The scaling relation derived in the present study links the timescale of the flow of an outlet glacier to its geometry, i.e. to the spatial dimensions of its lateral confinement, and to the temperature of the ice. Earlier work that dealt with the topic of confined outlet glacier flow includes analyses of the

60 dependency of ice flux and grounding-line dynamics on the confinement width and in-depth investigations of the role of lateral shear margins (e.g., Nye, 1965; Raymond, 1996; Joughin et al., 2004; Gudmundsson et al., 2012; Pegler et al., 2013; Haseloff et al., 2015; Schoof et al., 2017; Pegler, 2018). Laterally unconfined ice flow and its response time to small perturbations have been examined for a regime of low basal shear and driving stress in Sergienko and Wingham (2019).

  In a previous study we applied the similitude principle to the one-dimensional flow problem in combination with observa-
65 tional data, to compare the timescales of geometrically similar, MISI-prone Antarctic outlet glaciers (Levermann and Feldmann, 2019). This one-dimensional approach, however, neglected the important buttressing effect of the outlet's lateral confinement. Our present analysis respects the buttressing effect of the grounded ice portion through the width of the confinement as one of the dominant parameters determining the timescale of the ice dynamics. The derivation of the associated scaling relation is outlined in Sect. 2. It is then tested in Sect. 3, examining the scaling of 1) observed Greenland outlet-glacier flow speeds and
70 2) simulated Antarctic-type MISI retreat rates. In Sect. 4 we apply the scaling relation to a set of MISI-prone Antarctic outlet glaciers to compare their timescales, using a method that is principally similar to but more sophisticated than the one used in Levermann and Feldmann (2019) as we here extend it to both horizontal dimensions and carry out a more profound statistical analysis of the obtained outlet-specific scales. The limitations of our approach are discussed in Sect. 5 where we also draw our conclusions.

75 2 Derivation of the scaling relation

Our derivation of the scaling relation (detailed in Appendix A) is based on the shallow-shelf approximation of the Stokes stress balance of the ice (SSA; MacAyeal, 1989; Greve and Blatter, 2009). The SSA captures the dynamics of a fast and shallow ice flow and neglects vertical shearing inside the ice. Under the assumption that shear stresses between the ice and bed are low, the SSA describes a flow which is controlled by the balance between horizontal ice-internal stresses and the driving stress due to the surface gradient of the ice. Such conditions can be found in the grounding-line regions of the rapidly sliding ice-
80 stream outlets around Greenland and Antarctica, as indicated by inferred basal friction (Morlighem et al., 2013; Sergienko and Hindmarsh, 2013; Sergienko et al., 2014; Maier et al., 2019) and observed velocity data (Joughin et al., 2018; Mouginot et al., 2019). Typically, these ice streams are much longer than wide, thus exhibiting a small width-to-length ratio $R = W/L$, as the characteristic along-flow length scale L is typically observed to be a multiple of the width scale W (Morlighem et al., 2017;
85 Mouginot et al., 2019; Morlighem et al., 2020). Without loss of generality we place the two horizontal axes of the coordinate system of our analysis into the main flow direction ($\parallel$) and perpendicular ($\perp$) to it (Fig. 1). Using this information in a simple dimensional analysis of the SSA, in which all quantities have been non-dimensionalized (Appendix A), the stress balance

reduces to

$$\lambda \partial_\perp [H(\partial_\perp v_\parallel)^{\frac{1}{n}}] = H\partial_\parallel h, \tag{1}$$

90   with

$$\lambda = [(2AT)^{\frac{1}{n}} \rho g D R^{\frac{1}{n}+1}]^{-1}, \tag{2}$$

where $v_\parallel$ is the ice speed along the main flow direction and thereby along the bed trough, H is the ice thickness, h represents the surface elevation of the ice, n is Glen's flow law exponent determining the ice rheology (Greve and Blatter, 2009), and $\partial_\parallel$ and $\partial_\perp$ denote the spatial derivatives parallel and perpendicular to the main flow direction, respectively. Notably, Eq. (1) is

95   determined by a single dimensionless coefficient λ, in which A is the ice softness, D and T represent the characteristic vertical length scale and the timescale of the system, respectively, ρ denotes the ice density and g is the gravitational acceleration. The coefficient λ represent the balance between 1) the leading-order ice-internal stress, i.e., the horizontal shearing of the ice flow in across-trough direction and 2) the driving stress of the ice, which is determined by the surface gradient along the trough. As long as λ remains constant, the ratio of these two stresses will remain the same, while the characteristic scales of the system are

100   allowed to vary. In other words, the ice dynamics of the considered system will remain similar under a scaling of the system that leaves the system's governing dimensionless number λ unchanged (concept of similitude). Considering a reference system and applying a scaling to it (denoted by a dash), the requirement of $\lambda' = \lambda$ then yields a time-scaling relation that assures the similitude of the two systems:

$$\tau = \alpha^{-1}\beta^{-n} \left(\frac{\omega}{\delta}\right)^{-(n+1)}. \tag{3}$$

105   Here $\tau = T'/T$ is the ratio of the timescales, $\alpha = A'/A$ denotes the scaling of the ice softness, and $\beta = D'/D$, $\omega = W'/W$ and $\delta = L'/L$ represent the scaling of the confinement depth, width and length, respectively (Fig. 1, Table 1). Observations and laboratory studies yield a range of possible values for n ranging from 2 to 4 (e.g., Schoof, 2007; Haseloff et al., 2015; Greve and Blatter, 2009; Cuffey and Paterson, 2010). Using the most commonly applied value of $n = 3$ we obtain

$$\tau = \alpha^{-1}\beta^{-3}\gamma^{-4}, \tag{4}$$

110   where $\gamma = \omega/\delta = R'/R$ expresses the scaling of the horizontal aspect ratio (width-to-length ratio) of the confinement. The timescale is thus a strongly non-linear function of the spatial dimensions of the confinement, i.e., decreasing with the fourth power of its width-to-length ratio and with the third power of the bed depth. Furthermore, the timescale is inversely related to the ice softness which means that higher ice temperatures lead to a faster timescale. This is due to the fact that a higher softness enhances the deformation rate of the ice (Cuffey and Paterson, 2010), reducing the restraint due to lateral shear and promoting

115   along-flow extension of the ice, both inducing faster ice flow and discharge. The different characteristics of the geometry will generally have influences along the following lines: A deeper bed trough might imply a stronger ice gradient at the grounding line for similar glaciers, and thereby a stronger driving stress. In case of a MISI-type retreat, a shorter horizontal length scale, i.e., a steeper retrograde bed slope, leads to a higher flux increase for each increment of grounding-line retreat down the slope,

hence amplifying the positive feedback loop between ice discharge and retreat (Schoof, 2007; Pattyn and Morlighem, 2020).
120 A wider confinement diminishes the buttressing strength of the system (Dupont and Alley, 2005; Gudmundsson et al., 2012),
which in turn provides less moderation to the unstable retreat.

Using the confinement geometry, the time scaling τ (Eq. 3) can be translated into a scaling of the glacier outflow μ, i.e.,
the discharge through the confinement. For this purpose the velocity scaling $\nu = V'/V = \delta/\tau$ (based on the velocity scale
$V = L/T$) is multiplied with the scaling of the confinement depth β and width ω, respectively, yielding

125 $$\mu \equiv \nu\,\beta\,\omega = \frac{\delta\,\beta\,\omega}{\tau} = \alpha\,\beta^4\,\omega^5\,\delta^{-3} = \alpha\,\beta^4\,\gamma^5\,\delta^2. \qquad (5)$$

This serves as a measure for the relative outflow between individual outlets, i.e., the average velocity times the vertical outflow
area near the grounding line. Introducing the ratio of the depth gradients $\Gamma \equiv \beta/\delta$ this becomes

$$\mu = \alpha\,\delta\,\Gamma^4\,\omega^5, \qquad (6)$$

i.e., the outgoing volume flux scales linearly with the temperature and the bed depth, respectively, and with the fourth power of
130 the gradient of the bed topography and with the fifth power of the confinement width. Please note that the above relations only
hold under the listed assumptions, especially the assumption of geometric similarity, i.e., for glaciers that have qualitatively the
same topography only in different sizes.

3 Testing of the scaling relation

The analytically derived time-scaling relation (Eq. 4) is tested in two very different settings. First, we analyse observational
135 geometric and velocity data from strongly confined outlet glaciers in Greenland. Second, we investigate the time scaling of
simulated Antarctic-type MISI.

3.1 Observed velocity scaling of Greenland outlet glaciers

The Greenland Ice Sheet drains through many very narrow, fjord-type outlets, suggesting a particularly strong control of the
bed topography on the ice-flow timescale (Morlighem et al., 2017; Catania et al., 2020). We use a dataset from Beckmann et al.
140 (2019) which covers twelve outlet glaciers around Greenland (Figs. 2 and S1) to compare the observed relationship between
the ice-flow timescale and the confinement width of the outlets to the results predicted by theory (Eq. 3). The comparison with
the theory is only valid for observed glaciers that are approximately dynamically and geometrically similar, which excludes
two glaciers from the analysis (see Appendix B for details). Observations allow to directly use the velocity scale $V = L/T$ as
a time-scale measure, with velocity scaling $\nu = V'/V = \delta/\tau$. The geometry dependence of the velocity scaling according to
145 Eq. (3) reduces to

$$\nu = \omega^4, \qquad (7)$$

for $n = 3$ if differences in the width of the glaciers dominate the velocity field ($\alpha = \beta = \delta = 1$). This quartic relationship turns out to approximate the observed velocity-width scaling reasonably well (Fig. 3). Deviations from the predicted curve likely occur due to the fact that the comparison of the complex real-world glaciers breaks the underlying theoretical assumption

150 of perfect similarity. Deviations also result from differences between the individual glaciers in their ice softness fields, in the degree of non-linearity of their ice rheologies (flow-law exponent n) or in the vertical and along-flow geometry of their topographic confinements, which here are all assumed to be identical.

3.2 Modelled MISI time scaling with idealized geometry

The scaling relation (Eq. 4) applies to the *timescale of glacier flow*, as supported by the comparison with observations of

155 Greenland outlet glaciers of similar geometry in the previous section. This flow timescale is linked to the ice discharge across the grounding line, since a faster coastal flow, i.e., a smaller τ, implies a larger grounding-line discharge μ (Eq. 5). Grounding-line retreat depends on the divergence of grounding-line discharge, i.e., on the divergence of the flow speed at the grounding line. If we were to seek a relation for the grounding-line retreat, we could make the assumption that the retreat speed of an outlet glacier is proportional to its flow speed. This is a strong assumption and it might not be justified in all cases. Under this

160 assumption the *timescale of glacier retreat* would be proportional to the *timescale of glacier flow*. This would mean that Eq. (4) would also be applicable to the time scaling of glacier retreat.

To test this assumption we simulate the timescale of MISI-type outlet-glacier retreat under a systematic variation of each of the variables involved in Eq. (4) in an ensemble of idealized, three-dimensional numerical experiments. For this purpose we employ the Parallel Ice Sheet Model (PISM; Bueler and Brown, 2009; Winkelmann et al., 2011; Khroulev and Authors, 2020).

165 The model solves the full SSA equations (Eq. A1) of the stress balance from which the above scaling relation is derived, thus accounting for all the horizontal compressive, tensile and shear stresses that act within the ice as well as basal shearing.

The bed topography prescribed in the simulations is obtained and modified from the MISMIP+ intercomparison project, which is the current benchmark for idealized simulations of a buttressed marine ice-sheet-shelf system (Asay-Davis et al., 2016; Cornford et al., 2020; Lhermitte et al., 2020; Zhang et al., 2020; Leguy et al., 2021; Feldmann et al., 2022). It shapes a

170 trough with a retrograde bed section (Fig. 4), resembling the geometric characteristics of a deeply incised, MISI-prone marine Antarctic outlet such as Pine Island Glacier. Ice flow in this setup mainly takes place from the interior through the bed trough, where an ice stream feeds a bay-shaped ice shelf that calves into the ocean (Fig. S2). There is also a perpendicular flow component, i.e., from the channel's lateral ridges down into the trough. Resulting convergent flow and associated horizontal shearing (Fig. S3) enable the emergence of buttressing. Details on the model setup and the experimental design are given in

175 Appendix C.

In our simulations we vary separately the four relevant parameters which are found to determine the timescale of the ice dynamics according to Eq. (4). That is, the depth D, the width W and the length L of the bed trough and the ice temperature T_{ice} (ice softness $A(T_{\mathrm{ice}})$; see Eq. C1) are altered one at a time (see Table 2 for parameter ranges). The timescale T is measured

as the time per km of grounding-line retreat (inverse retreat speed) down the central part of the retrograde bed section (marked
grey in Fig. 5). This way we obtain four sets of simulations, i.e., for the ice-softness scaling α, the confinement-depth scaling
β, the length scaling δ and the width scaling ω, each of them yielding a curve for the time scaling τ (large panels in Fig. 6).
To examine the scaling behavior of the measured retreat timescales, we normalize each set of simulations with respect to the
same reference softness / confinement depth / confinement length / confinement width and the associated reference timescale.
In each of the resulting scaling diagrams (insets in Fig. 6) the numerical results are in good agreement with our analytically
derived time-scaling relation of Eq. (4).

Note that the uniformness of the basal friction coefficient C in space and time leads to simulated basal shear stresses that
are generally non-zero throughout the computational domain. Our analytical derivation of the scaling relation (Eq. 4) and its
application to observations assume negligible basal stresses close to the grounding line. Therefore, we carried out a separate
set of simulations with strongly reduced uniform values of C. The results suggest that while the *absolute* timescale of retreat
varies with the friction coefficient, the *scaling* of the retreat time still obeys the theoretical scaling relation (Fig. S4). In our
experiments a reduction of C of more than one order of magnitude leads to an outlet glacier of pronounced flatness compared
to the parabolic profile of the reference simulation and thus violates the similarity principle.

An additional set of experiments of altered accumulation rate a is conducted to analyze how a scaling of the surface mass
balance affects the time scaling of grounding line movement. The simulations yield a slightly larger or smaller ice sheet
depending on whether the accumulation rate is increased or decreased. This in turn slightly changes the depth, length and
width measurements of our analysis and thereby the timescale. Figure S5 shows that the changes induced by the relative
accumulation changes have a relatively weak influence on the timescale.

4   Application of scaling relation to Antarctic outlet glaciers

Our analysis of observed Greenland outlet-glacier velocities revealed that their scaling follows the theoretical prediction from
the scaling relation (Sect. 3.1; Fig. 3). The validity of the scaling relation is further supported by the conducted ensemble of
idealized, numerical simulations of Antarctic-type outlet-glacier retreat (Sect. 3.2), as simulated MISI retreat timescales are in
good agreement with the ones predicted from theory (Fig. 6). This leads us to apply the theory to observations of Antarctica's
MISI-prone outlet glaciers to compare their retreat timescales after a potential destabilization. We base our approach on the
fact that the currently observed geometry and physical conditions of the considered outlet glaciers represent the balance of the
relevant forces that act on the ice. This static situation carries the information for their initial retreat timescale after a potential
destabilization.

Analyzing the major outlets around Antarctica, we find 13 glaciers that show a clear retrograde bed slope upstream of
their grounding line and have a generally similar bed profile. Please confer Supplementary Figures S9-S23 for maps of the
topographic features of each glacier and Appendix D1 for a definition of the applied similarity criteria. These glaciers are

210 situated in the Amundsen Sea Sector, East Antarctica and the Filchner-Ronne region (Fig. 7). The three geometric scales required by Eq. (4), i.e., the depth, width and length scales are obtained from the recent BedMachine Antarctica compilation (Morlighem et al., 2020). The ice softness (Fig. S8), entering the scaling relation as the fourth parameter, is obtained from a present-day simulation of the Antarctic Ice Sheet, which was conducted in the course of the recent ISMIP 6 Antarctica intercomparison project (Seroussi et al., 2020). Pine Island Glacier (PIG) is selected as the scaling reference for our analysis.

215 It is one of the most studied glaciers in Antarctica and might have been destabilized by recent oceanic warming. The scales are extracted along the streamlines of each outlet (Figs. S9-S23, panels A,C and D), based on the MEaSUREs Antarctic velocity map from Mouginot et al. (2019). From this we obtain probability distributions of the respective scaling ratios (Figs. S9-S23, panel E), representing the spatial variability of the extracted data. The distributions of the retreat-time scaling (Fig. 8) are calculated according to Eq. (4) using a Monte Carlo method. The medians of these distributions, $<\tau>$, represent the best

220 estimate of our calculations. Details on our method and the underlying datasets are given in Appendix D.

The obtained timescales range over three orders of magnitude (Fig. 7 and Table 3), mainly due to differences in the bed-slope magnitude (length scale), the width of the confinement and its depth, as these scales enter Eq. (4) by the power of 3 and 4, respectively. Below we will refer to the inverse values of the time-scaling estimates, i.e., $<\tau>^{-1}$, providing a measure of the glaciers' potential retreat speed relative to the reference PIG.

225 By far the fastest retreat speed after a potential destabilization is detected for Mellor Glacier (MG; $<\tau_{\mathrm{MG}}>^{-1} = 67$). Here the slowing influence of its relatively narrow confinement is strongly overcompensated by the combination of a deep trough (about 2000 m; together with Foundation Ice Stream (FIS) the deepest of the ensemble, see Table 3 and Fig. S7) and a steep retrograde bed slope (with about -55 m/km the steepest of the entire ensemble). The fast retreat speed of Ninnis Glacier (NG; $<\tau_{\mathrm{NG}}>^{-1} = 20$) is primarily caused by its relatively steep retrograde slope. Similar retreat rates are obtained for the outlets

230 of Thwaites Glacier (TG; $<\tau_{\mathrm{TG}}>^{-1} = 19$) and Cook Glacier (CG; $<\tau_{\mathrm{CG}}>^{-1} = 16$), which is for different reasons: While CG has the widest confinement among all investigated outlets (100 km), being almost twice as wide as TG's confinement, its retrograde slope is only half as steep compared to the slope of TG. Both effects roughly balance out and since the scaling ratios for the ice softness and the trough depth are very similar, respectively, this leads to the similar timescale. The reference glacier of our analysis, PIG, is found to have a much slower retreat speed. The effect of having the second softest ice of all

235 examined outlets is outdone by the glacier's comparatively gentle slope and narrow trough, respectively. Slower retreat rates are only found for Recovery Glacier (RG; $<\tau_{\mathrm{RG}}>^{-1} = 0.8$; slightly narrower, flatter bed trough) and FIS ($<\tau_{\mathrm{FIS}}>^{-1} = 0.1$; much flatter slope). Smith Glacier and Denman Glacier show a pronounced bimodal time-scale distribution (highlighted in Fig. 8) which is an imprint of their bimodal distributions: for both glaciers the inferred depth scales D span a relatively large range and cluster around the two endings of it, revealing two distinct depth regimes at the grounding line (Figs. S10 and

240 S13). For some glaciers the likely ranges of τ are very large, which is a combined effect of 1) our method of extracting the characteristic scales, capturing the full spatial variability inside the confinement and 2) the high degree of non-linearity of the scaling relation, amplifying the uncertainty in the obtained scaling ratios. Note that we do not account for the uncertainty of the underlying topographic data itself. As the density of measurements is relatively high over many of the Antarctic outlet glaciers,

the vertical accuracy over the regions considered in this study is typically on the order of ~ 10 m, lying at the very low end of
the overall Antarctic uncertainty range (Morlighem et al., 2020).

Despite having the fastest timescale, the sea-level contribution of a potential retreat of MG could be comparatively small
(Fig. 7). For instance, the volume of marine ice in the drainage basin of Slessor Glacier (SLG) / RG and CG / NG is more than
2.5 as large compared to the basin of MG. The consequences of a destabilization could thus be more serious for CG, NG and
Support Force Glacier (SFG) as these tributaries show both a high retreat speed and a large sea-level potential.

5   Discussion and conclusions

Exploiting the similitude principle, we derived a time-scaling relation for the case of fast, shallow, and laterally confined
outlet-glacier flow with negligible basal friction (Eq. 4). According to this relation, the timescale of an outlet is proportional
to the inverse of its ice temperature and highly non-linearly related to the width, length and depth scales of its confinement,
respectively. That is, deeper and wider outlets with a steeper retrograde slope have a faster timescale than shallower, more
confined outlets with a flatter slope (Fig. 1). We showed that the derived scaling relation is able to predict the scaling of 1)
observed flow velocities of Greenland outlet glaciers (Sect. 3.1; Fig. 2) and 2) Antarctic-type MISI retreat speed as simulated
in idealized experiments (Sect. 3.2; Fig. 6). Motivated by these simulations, we applied the scaling relation to the observed
topography of 13 MISI-prone Antarctic outlets to compare their time scaling of potential unstable retreat (Sect. 4; Fig. 7).
Within this set of outlets, Mellor, Ninnis, Thwaites, Cook Glaciers have the fastest timescales - about 16 to 67 times faster
than the reference Pine Island Glacier (Fig. 8; Table 3) - due to their particularly wide and/or deep confinements and/or steep
slopes (Figs. S7 and S9-S23). The underlying approach and its application have several limitations which restrict the results
with respect to:

1.   **Similitude requirement:** The application of Eq. (4) to observed glaciers is limited by the requirement of geometric
     similarity. That is to say that the approach can only be used to compare existing outlet glaciers if they can be scaled
     onto each other as shown in the Supplementary figures (Figs. S9-S23, panel A). Effects of differences in ice-shelf
     buttressing or smaller topographic differences such as ice rises and details in the bed topography can alter the timescale
     of different glaciers in a way that cannot be captured by the approach because it weakens the similitude assumption.
     Perfect geometric similarity between two systems can only be achieved in a synthetic environment, i.e., in idealized
     experiments such as the ones carried out in this study to test the scaling relation (Sect. 3.2). The results from our
     numerical simulations suggest that the scaling relation is valid for strictly similar geometries (Fig. 6). The real-world
     glaciers considered here show geometric similarity in a broader sense. Dissimilarities between the glaciers are reflected
     in the uncertainty ranges of the obtained time scaling ratios (Table 3).

2.   **Region of applicability:** Our analysis is restricted to regions in which basal shear stresses are small compared to the ice-
     internal stresses (including the buttressing-inducing lateral shear stresses). This assumption generally holds for coastal
     regions of most Antarctic outlet glaciers where basal shear stresses are found to be close to zero (Joughin et al., 2004;

Morlighem et al., 2013; Sergienko and Hindmarsh, 2013; Sergienko et al., 2014) - with the possibility of the sporadic occurrence of confined and comparatively small rib-like patterns of high basal resistance in some areas (Sergienko and Hindmarsh, 2013; Sergienko et al., 2014). The region of low basal friction is likely to follow the grounding line in case of retreat as the lubrication of the bed is largely caused by the abundance of liquid water at the base of the ice sheet (Cuffey and Paterson, 2010). Therefore, we carried out a separate set of simulations with strongly reduced uniform values of C. The results suggest that while the *absolute* timescale of retreat varies with the friction coefficient, the *scaling* of the retreat time still obeys the theoretical scaling relation (Fig. S4).

3. **Time period of applicability:** In principle the applicability of our analysis is also limited by possible changes in surface mass balance. These are, however, likely slower than the ice-dynamic discharge. Estimates of the past decades show a background snowfall in coastal regions of at most 1 m/yr (Wessem et al., 2014; Agosta et al., 2019). Changes in this quantity can be estimated by a $5-7$ % increase for every degree of warming in the atmosphere (Frieler et al., 2015) and are thus on the order of $0.05-0.7$ m/yr/K. Differences in the surface mass balance between individual outlets are modeled to be on the order of 0.1 m/yr (Wessem et al., 2014; Agosta et al., 2019). In contrast, the highest observed dynamic thinning rates of the destabilized outlets in West Antarctica's Amundsen Sea Sector typically reach up to $5-10$ m/yr (Konrad et al., 2018; Pritchard et al., 2009; Shepherd et al., 2019), making changes in the surface mass balance a second-order effect with respect to the retreat timescale. Observed average grounding-line retreat rates of these outlets reach up to 1 km/yr (Rignot et al., 2014; Konrad et al., 2018) from which we estimate that our results may be valid for at least two decades after a potential destabilization. After that the analysis might have to be updated with the altered topography. A comparison of our numerical scaling results (insets of Fig. 6) to an additional set of simulations of altered surface accumulation yields that a scaling of the surface mass balance has a relatively weak influence on the time scaling of grounding-line retreat (Fig. S5).

Within these very strong constraints the scaling relation can capture dependencies of highly complex stress- and flow fields. It resolves the buttressing effect of the grounded portion of an outlet explicitly, by extracting its dependence on the geometry of the outlets' grounded lateral confinement. In our analysis we infer the associated characteristic scales upstream of the grounding line focusing on the retrograde bed section as the crucial region that determines the timescale of a potential instability and thus we do not take into account the ice-shelf geometry. In our simulations the ice shelves and the upstream confinement share the same width scale (Figs. 4 and S2). The outlets feeding the large Filchner-Ronne Ice Shelf deviate from this assumption. They might respond on a slower timescale than inferred here due to the stabilizing influence of the large ice rises and other smaller pinning points in the central region of the ice shelf and the convergent flow of at least ten ice streams that enter the ice shelf, effects that cannot be accounted for by our approach.

For the majority of outlets analyzed here, a comparison of the bed topography and the ice-flow pattern suggests a strong control of the bed topography on the width of the outlet (e.g., Pine Island Glacier, Denman Glacier, Mellor Glacier or Slessor Glacier; Figs. S9, S13, S15, S16; visualized schematically in Fig. 1). That is, the lateral margins of these glaciers are clearly defined by the lateral ridges of the underlying bed trough. However, a few glaciers (e.g., Thwaites Glacier and Ninnis Glacier;

310   Figs. S9 and S12) reveal a much weaker topographic control. We base the delineation of the outlets' lateral margins on the e-folding scale of their velocity field. While other methods of deducing the glacier-width scale may lead to different results in cases of weak topographic influence, our approach provides a well-defined width measure that can be applied consistently to all outlets, independent of their individual degree of topographic control.

     Outlets discarded in this study include Pope Glacier and Kohler Glacier (eastern and western branch). Though both troughs of
315   Kohler Glacier have a retrograde bed section upstream of the grounding line, their strongly undulating bed topography further upstream (Figs. S21 and S22) deviates substantially from the rest of the ensemble. Pope Glacier (Fig. S23) is excluded from our analysis due to its very short retrograde slope section (3 km). The main outlets feeding Ross Ice Shelf, e.g., Bindschadler Ice Stream and MacAyeal Ice Stream, and also Totten Glacier in East Antarctica, are found to have a generally, i.e. flux-weighted, flat or prograde bed topography upstream of the grounding line.

320   The timescales obtained here differ from the ones estimated in a previous study in which we also applied the similitude principle to Antarctic outlets (Levermann and Feldmann, 2019). This is due to the fact that the two studies make different assumptions in the dimensional analysis of the SSA leading to different scaling relations which yield different results. For instance, the one-dimensional analysis in Levermann and Feldmann (2019) does not account for the across-flow direction (y direction here) and thus neglects the effect of horizontal shearing. In the present study horizontal shear stresses turn out to
325   represent the most important stresses compared to all other ice-internal stresses, originating from the assumption of a generally small width-to-length ratio of Antarctica's outlet glaciers. In fact, the timescale of TG estimated here is about ten times faster than in the previous study, since the present study takes into account the much larger width of TG (and thus the smaller buttressing effect of its grounded portion) compared to the reference PIG. In contrast, in the present study basal stresses are neglected, whereas in Levermann and Feldmann (2019) there is a separate scaling law that involves basal friction parameter.
330   Furthermore, the present study uses a more sophisticated method of extracting the outlets' characteristic scales, i.e., they are extracted for each glacier along a set of streamlines spanning its confinement compared to a single linear central profile used in Levermann and Feldmann (2019). The method of extraction also has an influence on which glaciers are labeled as MISI prone, such that the ensembles of outlets for which we obtain time scaling values presented here and in our previous work are not the same. Such qualitative differences between the two studies naturally lead to different timescale estimates which should
335   be interpreted in the light of the underlying assumptions.

     The scaling approach presented here provides a useful tool that in particular allows to compare (MISI) timescales between similar glaciers within the limits of the underlying assumptions and constraints - without the need of computationally expensive numerical simulations. Further studies are required in particular to explore the role of ice-shelf buttressing on the time scaling, allowing for a more comprehensive scaling analysis.

340   *Code and data availability.* Antarctic bed topography and ice thickness are taken from the Bedmachine Antarctica compilation (MEaSUREs BedMachine Antarctica, Version 1) and can be downloaded from https://nsidc.org/data/NSIDC-0756/versions/1. Antarctic surface veloci-

Appendix A: Similitude analysis of shallow ice dynamics

We apply the concept of similitude (Buckingham, 1914; Rayleigh, 1915; Szücs, 1980) to the dynamics of ice sheets based
on the shallow-shelf approximation (SSA; Morland, 1987; MacAyeal, 1989) of the Stokes stress balance (Greve and Blatter,
2009). Neglecting the terms of vertical shearing in the stress balance and accounting for the small thickness-to-length ratio
350 of ice sheets, the SSA represents the relevant dynamics of floating ice shelves and grounded ice streams, characterized by
fast, plug-like flow. In particular, we assume isothermal ice, a condition that has been used to analyze ice-sheet dynamics in
a number of previous studies (e.g., Dupont and Alley, 2005; Goldberg et al., 2009; Gudmundsson et al., 2012; Pattyn et al.,
2013; Feldmann and Levermann, 2016; Seroussi and Morlighem, 2018; Cornford et al., 2020).

For an ice stream with horizontal velocity components v_x and v_y, ice thickness H, ice surface elevation h, and spatially
355 uniform (isothermal) ice softness A, the SSA has the following two horizontal components,

$$A^{-1/n}\left(\frac{\partial}{\partial x}\left[H\dot{\epsilon}_e^{1/n-1}\left(2\frac{\partial v_x}{\partial x}+\frac{\partial v_y}{\partial y}\right)\right]+\frac{1}{2}\frac{\partial}{\partial y}\left[H\dot{\epsilon}_e^{1/n-1}\left(\frac{\partial v_x}{\partial y}+\frac{\partial v_y}{\partial x}\right)\right]\right)+\tau_{b,x}=\rho g H\frac{\partial h}{\partial x},$$
$$A^{-1/n}\left(\frac{\partial}{\partial y}\left[H\dot{\epsilon}_e^{1/n-1}\left(2\frac{\partial v_y}{\partial y}+\frac{\partial v_x}{\partial x}\right)\right]+\frac{1}{2}\frac{\partial}{\partial x}\left[H\dot{\epsilon}_e^{1/n-1}\left(\frac{\partial v_y}{\partial x}+\frac{\partial v_x}{\partial y}\right)\right]\right)+\tau_{b,y}=\rho g H\frac{\partial h}{\partial y},$$

(A1)

where $\dot{\epsilon}_e$ is the effective strain rate, τ_b is the basal shear stress, ρ is the ice density, g the gravitational acceleration and n denotes
Glen's flow-law exponent (Cuffey and Paterson, 2010). The SSA implies that the horizontal velocities do not vary in vertical
(z) direction. Eqs. (A1) describe the balance between 1) ice-internal stresses due to shearing, extension and compression (in
360 large brackets), 2) the basal shear stress $\tau_b=(\tau_{b,x},\tau_{b,y})$ between ice and bed and 3) the driving stress due to the gradient in the
ice-surface elevation. Here we consider the case in which the driving stress is mainly balanced by the ice-internal stresses and
we will neglect the basal shear stress term in the following.

The effective strain rate $\dot{\epsilon}_e$ (Greve and Blatter, 2009) in Eqs. (A1) can be written as

$$\dot{\epsilon}_e=\left[\left(\frac{\partial v_x}{\partial x}\right)^2+\left(\frac{\partial v_y}{\partial y}\right)^2+\frac{\partial v_x}{\partial x}\frac{\partial v_y}{\partial y}+\frac{1}{4}\left(\frac{\partial v_x}{\partial y}+\frac{\partial v_y}{\partial x}\right)^2\right]^{1/2}.$$

(A2)

365 Introducing the geometric scales S_x and S_y as the two characteristic horizontal dimensions of the system and a timescale T, we
bring the components of the effective strain rate (Eq. A2) into dimensionless form via $v_x^*=\frac{v_x T}{S_x}$ and $v_y^*=\frac{v_y T}{S_y}$, which yields

$$\dot{\epsilon}_e=T^{-1}\left[\left(\frac{\partial v_x^*}{\partial x^*}\right)^2+\left(\frac{\partial v_y^*}{\partial y^*}\right)^2+\frac{\partial v_x^*}{\partial x^*}\frac{\partial v_y^*}{\partial y^*}+\frac{1}{2}\frac{\partial v_x^*}{\partial y^*}\frac{\partial v_y^*}{\partial x^*}+\frac{1}{4R^2}\left(\frac{\partial v_x^*}{\partial y^*}\right)^2+\frac{R^2}{4}\left(\frac{\partial v_y^*}{\partial x^*}\right)^2\right]^{1/2},$$

(A3)

with

$$R = \frac{S_y}{S_x}. \tag{A4}$$

370 Defining the dimensionless variables $H^* = \frac{H}{D}$ and $h^* = \frac{h}{D}$ with the vertical geometric scale D we now non-dimensionalize (Buckingham, 1914) the x-component of the SSA (Eqs. A1), writing

$$\frac{K}{T}\frac{\partial}{\partial x^*}\left[2H^*\dot{\epsilon}_e^{1/n-1}\frac{\partial v_x^*}{\partial x^*} + H^*\dot{\epsilon}_e^{1/n-1}\frac{\partial v_y^*}{\partial y^*}\right]$$
$$+\frac{K}{2T}\frac{\partial}{\partial y^*}\left[H^*\dot{\epsilon}_e^{1/n-1}\frac{1}{R^2}\frac{\partial v_x^*}{\partial y^*} + H^*\dot{\epsilon}_e^{1/n-1}\frac{\partial v_y^*}{\partial x^*}\right] = H^*\frac{\partial h^*}{\partial x^*}, \tag{A5}$$

with

$$K = \frac{1}{\rho g A^{1/n} D}. \tag{A6}$$

375 We specify that the main flow direction, i.e., along the topographic confinement, is in x direction and that the transversal, across-trough, flow component is in y direction (indicated by symbols $\parallel$ and $\perp$, respectively, in Eq. (1) in the main text). In this case, the two geometric horizontal scales can be associated with a length scale $L = S_x$ and a width scale $W = S_y$ of the confinement. Observations indicate that many of the outlet glaciers of Greenland and Antarctica stream through bed confinements with a characteristic length that is several times (in places one order of magnitude) larger than the confinement

380 width. Consequently, we assume $L \gg W$ and thus $R \ll 1$.

Accounting for the leading order term in the effective strain rate (Eq. A3), which is on the order of $\mathcal{O}(1/R^2)$, the effective strain rate can be approximated by

$$\dot{\epsilon}_e \approx \frac{1}{2RT}\frac{\partial v_x^*}{\partial y^*}. \tag{A7}$$

Analogous, in the SSA (Eq. A5) only the $1/R^2$ term remains on the left-hand-side of the equation. Using Eq. (A7), we can

385 eventually express the approximated SSA as

$$\lambda\frac{\partial}{\partial y^*}\left[H^*\left(\frac{\partial v_x^*}{\partial y^*}\right)^{1/n}\right] = H^*\frac{\partial h^*}{\partial x^*}, \tag{A8}$$

with

$$\lambda = \frac{K}{2^{1/n}T^{1/n}R^{1/n+1}}. \tag{A9}$$

Looking at Eq. (A8), we see that the stress balance remains exactly the same as long as the dimensionless coefficient λ remains

390 the same. In other words, the first-order ice-sheet dynamics of our problem are expected to be similar under a transformation that leaves this coefficient unchanged. Applying a scaling to the system (denoted by a dash) and requiring similarity ($\lambda' = \lambda$) yields

$$\frac{1}{A'D'^nT'}\left(\frac{L'}{W'}\right)^{n+1} = \frac{1}{AD^nT}\left(\frac{L}{W}\right)^{n+1}. \tag{A10}$$

Introducing the scaling ratios $\alpha = \frac{A'}{A}$, $\beta = \frac{D'}{D}$, $\omega = \frac{W'}{W}$, $\delta = \frac{L'}{L}$ and $\tau = \frac{T'}{T}$ for the geometric dimensions, the ice softness and

395   the timescale of the system, respectively, we arrive at

$$\tau = \alpha^{-1}\beta^{-n}\left(\frac{\omega}{\delta}\right)^{-(n+1)}. \tag{A11}$$

Since n is always positive, the timescale of the system will increase ($\tau > 1$) for a reduction of the ice-softness scale ($\alpha < 1$), a shortening of the vertical geometry ($\beta < 1$), an elongation of the geometry in main-flow direction ($\delta > 1$), or a narrowing of the across-main-flow geometry ($\omega < 1$). Defining $\gamma = R'/R = \omega/\delta$ and making the common choice of $n = 3$ (Greve and

400   Blatter, 2009; Cuffey and Paterson, 2010) we eventually obtain

$$\tau = \alpha^{-1}\beta^{-3}\gamma^{-4}. \tag{A12}$$

Appendix B: Analysis of Greenland outlet glaciers

The observational data used in our analysis is obtained from Beckmann et al. (2019) who inferred along-flow profiles of the bed elevation, ice thickness, ice velocity and glacier width for a selection of Greenland outlet glaciers based on flux-weighted

405   averages using geometric data from Morlighem et al. (2014) and velocity data from Rignot and Mouginot (2012). The twelve glaciers cover a variety of sizes, locations, discharge rates and climatic conditions across the Greenland Ice Sheet (Beckmann et al., 2019). At the same time most of these outlets are qualitatively similar to each other as their flow is strongly confined by a narrow lateral bed geometry and they are grounded on bedrock that is generally sloping up in landward direction (Figs. 2 and S1). Two glaciers deviating from these conditions, i.e., Daugaard-Jensen Glacier and Rink Glacier, are excluded from our

410   analysis. Daugaard-Jensen Glacier is the only outlet in the ensemble that is grounded on a landward down-sloping (instead of up-sloping) bed topography. It has been shown that these two types of bed slope can have fundamentally different effects on the ice-flow dynamics (Schoof, 2007). Rink Glacier exhibits a pronounced inversion of the ice-flow acceleration near the terminus, which might be due to a local specific topographic feature, making the outlet's ice-speed profile qualitatively very different compared to the rest of the outlets.

415   To extract a characteristic scale for the confinement width W of each of the individual glaciers we average the width profile over the first 60 km upstream of the glacier terminus. The same is done for the velocity scale V, though here leaving out the first 20 km to exclude the possible influence of ice-ocean interactions, i.e., melting and calving events, and their effects near the glacier terminus. The analysis of Gade Glacier, with its relatively short catchment, is limited to the first 40 km upstream of its terminus.

420   With the flow-speed scale $V = L/T$, the speed scaling ratio $\nu = V'/V$ can be written as

$$\nu = \frac{L'\,T}{L\,T'} = \delta\,\tau^{-1}. \tag{B1}$$

Assuming that both the time scaling and the velocity scaling of the considered glaciers are dominated by the width of their narrow topographic confinements ($\alpha = \beta = \delta = 1$) the analytically derived scaling relation (Eq. 4) reduces to

$$\tau = \omega^{-4}, \tag{B2}$$

425 and consequently

$$\nu = \omega^{4}, \tag{B3}$$

which provides a good approximation to the scaling behavior deduced from the observational data (Fig. 2).

Appendix C: Idealized simulations of MISI-type retreat

We apply PISM to a modified version of the MISMIP+ setup to simulate the unstable retreat of an inherently buttressed
430 Antarctic-type outlet glacier (Figs. 4 and S2). In the default MISMIP+ setting the model spinup yields a steady-state outlet glacier with a stable grounding-line position on the retrograde slope section of the bed (Asay-Davis et al., 2016; Cornford et al., 2020). A perturbation of this equilibrium leads to a reversible retreat of the outlet. That is, the triggered transient retreat stops and the grounding line migrates back toward its original equilibrium location once the perturbation ceases, even for strong perturbation magnitudes of basal ice-shelf melting or a reduction of the basal resistance (Gudmundsson et al., 2012; Cornford
435 et al., 2020). In order to be able to extract timescales of irreversible, i.e., MISI-type retreat, we widened and deepened the bed trough of the MISMIP+ setup. For a sufficiently wide trough, the outlet glacier that evolves after model initialization retreats down the entire retrograde slope, finding a stable equilibrium only on the landward up-sloping bed section close to the ice divide (reddish lines in Fig. 5). Using this experimental design, all of our conducted simulations share the same initial conditions (except for the varied parameter) and thus have a high degree of similarity, which facilitates the application of the
440 scaling to our numerical results.

The experiments are initiated from a block of ice of $2,000$ m thickness and are run into equilibrium for several $10,000$ model years. Ice surface accumulation due to snowfall takes place at a spatially uniform rate and is constant in time. Basal and surface melting of the ice are neglected. The temperature within the ice body, T_{ice}, is chosen to be uniform (isothermal) and is translated into an ice-softness value $A(T_{\text{ice}})$ by an Arrhenius law (Greve and Blatter, 2009; Cuffey and Paterson, 2010) of the
445 form

$$A(T_{\text{ice}}) = A_0 e^{-Q/R_g T_{\text{ice}}}, \tag{C1}$$

with constants A_0, Q and R_r (see Table 2).

For the grounded portion of the ice sheet the basal shear stress in Eqs. (A1), $\tau_b = (\tau_{b,x}, \tau_{b,y})$, is given by a Weertman-type sliding law (Greve and Blatter, 2009),

450 $$\tau_b = -C|v|^{m-1}v, \tag{C2}$$

with constant friction coefficient C and basal sliding exponent m. The parameter values used in the simulations are given in Table 2. The simulations are carried out on a regular horizontal grid of 2 km resolution, which assures adequate accuracy in modeling the rapid ice dynamics, as demonstrated by a convergence study (Fig. S6). In PISM, the grounding lines are diagnosed via the flotation criterion and thus evolve freely. Grounding line movement has been evaluated in the model intercomparison

455 projects MISMIP3d (Pattyn et al., 2013; Feldmann et al., 2014) and MISMIP+ (Cornford et al., 2020).

Appendix D: Measuring the Antarctic outlets

D1 Method

To apply the above derived theory to Antarctica's outlet glaciers, their characteristic scales involved in Eq. (4) have to be extracted from observations. To this end, for each outlet first we define a grounding-line section that spans the glacier's main

460 trunk, i.e., the part of the grounding line across which the vast majority of the glacier's total ice discharge takes place. Then, based on the velocity field of the ice, we infer the glacier's streamlines that meet this grounding-line section. The sampling resolution between and along the streamlines is 1 km. The flux-weighted average of the outlet's bed profile over all streamlines provides a general start point (p_1) and end point (p_2) of its retrograde bed section directly upstream of the grounding line (exemplary indicated in Fig. S9). For each streamline the confinement depth D is then measured as the depth of the bed below

465 zero at location p_1. The bed-slope magnitude S between p_1 and p_2 for each of the streamlines that have a negative mean slope inside this range provides the length scale L: If one compares two linear retrograde slopes of different magnitude over the same vertical distance, then the steeper slope passes this vertical distance over a shorter horizontal distance and thus has a shorter length scale than the shallower slope. This length scale is proportional to the inverse of the slope magnitude. The confinement width W is measured in perpendicular direction to a central streamline of the outlet (indicated in black in Figs. S9-S23) as

470 the distance at which the ice-flow speed has declined to the e-th fraction of the respective centerline value. This method of detecting the glacier's lateral shear margins facilitates the localization of its lateral boundary especially if the outlet is rather weakly confined by the bed topography (e.g., Thwaites Glacier, Fig. S9). For outlets that are instead sharply confined by the bed (e.g., Pine Island Glacier) the velocity-deduced shear margins agree well with the lateral topographic confinement (Fig. S9). The values for W are obtained along the first 20 km upstream of p_1. Over the same range the ice softness A is averaged for

475 each streamline. The above approach yields a set of measurements for each characteristic scale, spanning the observational range of this scale.

To ensure similarity between the measured outlets and comparability of their timescales via Eq. (4) we apply the following three criteria:

1. The outlets have to show **ice-stream characteristics**: the maximum flow speeds of the grounded part of the glacier have
480 to be at least 100 m/yr (most of them are streaming at >500 m/yr).

2. **MISI susceptibility**: within the first 20 km upstream of the grounding line the calculated flux-averaged bed profile has to be below sea level and it has to continuously slope down in landward direction over a distance of at least 5 km (the vast majority of the analyzed glaciers has an initial retrograde bed section of 10 km or more).

3. **General geometric similarity**: while each glacier's profile has of course its own characteristics we require that fluctuations in the bed-slope direction have to be modest, i.e., we discard glaciers with more than one pronounced peak in the bed profile within the first 20 km (which excludes the strongly undulating Kohler Glacier tributaries from our analysis).

Applying these criteria, we obtain an ensemble of 13 outlet glaciers around Antarctica that are suitable to be involved in our analysis. Note that since the choice of the similarity criteria is not unique a different set of criteria than the one used here may lead to a different ensemble of outlets.

We choose Pine Island Glacier as the reference system for calculating the scaling ratios α, β, δ and ω that enter the time-scaling relation. That is, the scales of all outlets analyzed in this study are expressed relatively to the scales of this reference. Pine Island Glacier is one of the most prominent Antarctic outlets and it is relatively well observed. Due to the nature of the conducted scaling analysis the scales calculated here could also be expressed relative to any other of the examined outlets without changing the results. Each scaling ratio of a specific glacier is considered as a distribution of results comprising all possible combinations of the two involved scales (of the specific glacier and the reference) in order to account for their uncertainty. The distribution for the time scaling ratio τ is then calculated according to Eq. (4), based on the likely range (range between the 17th and 83rd percentiles) of the distributions of α, β, δ and ω by conducting Monte-Carlo simulations with a sample size of 1000 (Fig. 8). Due to the large uncertainty in the observed along-flow bed shape (Morlighem et al., 2020) and the associated relatively large spread in the length scale, the δ scaling ratio is exempt from the Monte Carlo method and the median of the distribution is used in Eq. (4) instead.

D2 Underlying datasets

The characteristic scales of the outlet glaciers are all obtained from datasets that represent present-day conditions of the Antarctic Ice Sheet. The bed topography stems from the Bedmachine Antarctica dataset (Morlighem et al., 2020) from which we infer the outlet-specific geometric scales D, L and W. The regularly updated, continent-wide compilation involves data from various sources, including satellite, airborn radar, over-snow radar and seismic-sounding measurements. The novel dataset applies a mass conservation method to overcome limitations of the earlier BEDMAP2 compilation (Fretwell et al., 2013), revealing previously unkown bed features of Antarctica's outlets with substantial implications regarding their susceptibility to MISI.

Due to the absence of observed Antarctic ice-softness data, we use results from a present-day, continental-scale simulation of the Antarctic Ice Sheet, conducted with PISM in the course of the recent ISMIP 6 Antarctica intercomparison project (Seroussi et al., 2020). The thermo-mechanically coupled model is run into equilibrium under present-day conditions at a horizontal resolution of 8 km and a vertical resolution that ranges from 13 m at the ice base to 100 m at the top of the numerical domain.

As part of solving the stress balance of the ice, PISM computes a temperature-dependent ice softness field, from which the vertically averaged form serves as the underlying dataset for our inference of the ice-softness scale A (Fig. S8).

The ice flow field used to track the streamlines of the individual outlet glaciers is taken from Mouginot et al. (2019). It is
515 the most recent and precise dataset of the present-day Antarctic ice surface velocity, derived by applying a combination of interferometric phase-mapping and speckle-tracking techniques to satellite measurements from the last 25 years.

Author contributions. Both authors designed the study, developed the theory and wrote the paper. JF conducted the model simulations and prepared the figures.

Competing interests. The authors declare that they have no competing interests.

520 *Acknowledgements.* This work was supported by the Deutsche Forschungsgemeinschaft (DFG) in the framework of the priority programme "Antarctic Research with comparative investigations in Arctic ice areas" through grant LE 1448/8-1. We acknowledge the European Regional Development Fund (ERDF), the German Federal Ministry of Education and Research, and the Land Brandenburg for supporting this project by providing resources on the high-performance computer system at the Potsdam Institute for Climate Impact Research. Development of PISM is supported by NSF grants PLR-1644277 and PLR-1914668 and NASA grants NNX17AG65G and 20-CRYO2020-0052.

References

Agosta, C., Amory, C., Kittel, C., Orsi, A., Favier, V., Gallée, H., van den Broeke, M. R., Lenaerts, J. T. M., van Wessem, J. M., van de Berg, W. J., and Fettweis, X.: Estimation of the Antarctic Surface Mass Balance Using the Regional Climate Model MAR (1979–2015) and Identification of Dominant Processes, The Cryosphere, 13, 281–296, https://doi.org/10.5194/tc-13-281-2019, 2019.

Asay-Davis, X. S., Cornford, S. L., Durand, G., Galton-Fenzi, B. K., Gladstone, R. M., Gudmundsson, G. H., Hattermann, T., Holland, D. M., Holland, D., Holland, P. R., Martin, D. F., Mathiot, P., Pattyn, F., and Seroussi, H.: Experimental Design for Three Interrelated Marine Ice Sheet and Ocean Model Intercomparison Projects: MISMIP v. 3 (MISMIP +), ISOMIP v. 2 (ISOMIP +) and MISOMIP v. 1 (MISOMIP1), Geoscientific Model Development, 9, 2471–2497, https://doi.org/10.5194/gmd-9-2471-2016, 2016.

Bamber, J. L., Oppenheimer, M., Kopp, R. E., Aspinall, W. P., and Cooke, R. M.: Ice Sheet Contributions to Future Sea-Level Rise from Structured Expert Judgment, Proceedings of the National Academy of Sciences, 116, 11 195–11 200, https://doi.org/10.1073/pnas.1817205116, 2019.

Beckmann, J., Perrette, M., Beyer, S., Calov, R., Willeit, M., and Ganopolski, A.: Modeling the Response of Greenland Outlet Glaciers to Global Warming Using a Coupled Flow Line–Plume Model, The Cryosphere, 13, 2281–2301, https://doi.org/10.5194/tc-13-2281-2019, 2019.

Buckingham, E.: On Physically Similar Systems; Illustrations of the Use of Dimensional Equations, Physical Review, 4, 345–376, https://doi.org/10.1103/PhysRev.4.345, 1914.

Bueler, E. and Brown, J.: Shallow Shelf Approximation as a "Sliding Law" in a Thermomechanically Coupled Ice Sheet Model, Journal of Geophysical Research, 114, https://doi.org/10.1029/2008JF001179, 2009.

Catania, G. A., Stearns, L. A., Moon, T. A., Enderlin, E. M., and Jackson, R. H.: Future Evolution of Greenland's Marine-Terminating Outlet Glaciers, Journal of Geophysical Research: Earth Surface, 125, https://doi.org/10.1029/2018JF004873@10.1002/(ISSN)1944-9208.GRANDCHAL1, 2020.

Cornford, S. L., Seroussi, H., Asay-Davis, X. S., Gudmundsson, G. H., Arthern, R., Borstad, C., Christmann, J., Dias dos Santos, T., Feldmann, J., Goldberg, D., Hoffman, M. J., Humbert, A., Kleiner, T., Leguy, G., Lipscomb, W. H., Merino, N., Durand, G., Morlighem, M., Pollard, D., Rückamp, M., Williams, C. R., and Yu, H.: Results of the Third Marine Ice Sheet Model Intercomparison Project (MISMIP+), The Cryosphere, 14, 2283–2301, https://doi.org/10.5194/tc-14-2283-2020, 2020.

Cuffey, K. M. and Paterson, W. S. B.: The Physics of Glaciers, Academic Press, 2010.

DeConto, R. M., Pollard, D., Alley, R. B., Velicogna, I., Gasson, E., Gomez, N., Sadai, S., Condron, A., Gilford, D. M., Ashe, E. L., Kopp, R. E., Li, D., and Dutton, A.: The Paris Climate Agreement and Future Sea-Level Rise from Antarctica, Nature, 593, 83–89, https://doi.org/10.1038/s41586-021-03427-0, 2021.

Diener, T., Sasgen, I., Agosta, C., Fürst, J. J., Braun, M. H., Konrad, H., and Fettweis, X.: Acceleration of Dynamic Ice Loss in Antarctica From Satellite Gravimetry, Frontiers in Earth Science, 9, 2021.

Dupont, T. K. and Alley, R. B.: Assessment of the Importance of Ice-Shelf Buttressing to Ice-Sheet Flow, Geophysical Research Letters, 32, https://doi.org/10.1029/2004GL022024, 2005.

Edwards, T. L., Nowicki, S., Marzeion, B., Hock, R., Goelzer, H., Seroussi, H., Jourdain, N. C., Slater, D. A., Turner, F. E., Smith, C. J., McKenna, C. M., Simon, E., Abe-Ouchi, A., Gregory, J. M., Larour, E., Lipscomb, W. H., Payne, A. J., Shepherd, A., Agosta, C., Alexander, P., Albrecht, T., Anderson, B., Asay-Davis, X., Aschwanden, A., Barthel, A., Bliss, A., Calov, R., Chambers, C., Champollion, N., Choi, Y., Cullather, R., Cuzzone, J., Dumas, C., Felikson, D., Fettweis, X., Fujita, K., Galton-Fenzi, B. K., Gladstone, R., Golledge,

N. R., Greve, R., Hattermann, T., Hoffman, M. J., Humbert, A., Huss, M., Huybrechts, P., Immerzeel, W., Kleiner, T., Kraaijenbrink, P., Le Clec'h, S., Lee, V., Leguy, G. R., Little, C. M., Lowry, D. P., Malles, J.-H., Martin, D. F., Maussion, F., Morlighem, M., O'Neill, J. F., Nias, I., Pattyn, F., Pelle, T., Price, S. F., Quiquet, A., Radić, V., Reese, R., Rounce, D. R., Rückamp, M., Sakai, A., Shafer, C., Schlegel, N.-J., Shannon, S., Smith, R. S., Straneo, F., Sun, S., Tarasov, L., Trusel, L. D., Van Breedam, J., van de Wal, R., van den Broeke, M., Winkelmann, R., Zekollari, H., Zhao, C., Zhang, T., and Zwinger, T.: Projected Land Ice Contributions to Twenty-First-Century Sea Level Rise, Nature, 593, 74–82, https://doi.org/10.1038/s41586-021-03302-y, 2021.

Favier, L., Durand, G., Cornford, S. L., Gudmundsson, G. H., Gagliardini, O., Gillet-Chaulet, F., Zwinger, T., Payne, A. J., and Le Brocq, A. M.: Retreat of Pine Island Glacier Controlled by Marine Ice-Sheet Instability, Nature Climate Change, 4, 117–121, https://doi.org/10.1038/nclimate2094, 2014.

Feldmann, J. and Levermann, A.: Similitude of Ice Dynamics against Scaling of Geometry and Physical Parameters, The Cryosphere, 10, 1753–1769, https://doi.org/10.5194/tc-10-1753-2016, 2016.

Feldmann, J., Albrecht, T., Khroulev, C., Pattyn, F., and Levermann, A.: Resolution-Dependent Performance of Grounding Line Motion in a Shallow Model Compared with a Full-Stokes Model According to the MISMIP3d Intercomparison, Journal of Glaciology, 60, 353–360, https://doi.org/10.3189/2014JoG13J093, 2014.

Feldmann, J., Reese, R., Winkelmann, R., and Levermann, A.: Shear-Margin Melting Causes Stronger Transient Ice Discharge than Ice-Stream Melting in Idealized Simulations, The Cryosphere, 16, 1927–1940, https://doi.org/10.5194/tc-16-1927-2022, 2022.

Fretwell, P., Pritchard, H. D., Vaughan, D. G., Bamber, J. L., Barrand, N. E., Bell, R., Bianchi, C., Bingham, R. G., Blankenship, D. D., Casassa, G., Catania, G., Callens, D., Conway, H., Cook, A. J., Corr, H. F. J., Damaske, D., Damm, V., Ferraccioli, F., Forsberg, R., Fujita, S., Gim, Y., Gogineni, P., Griggs, J. A., Hindmarsh, R. C. A., Holmlund, P., Holt, J. W., Jacobel, R. W., Jenkins, A., Jokat, W., Jordan, T., King, E. C., Kohler, J., Krabill, W., Riger-Kusk, M., Langley, K. A., Leitchenkov, G., Leuschen, C., Luyendyk, B. P., Matsuoka, K., Mouginot, J., Nitsche, F. O., Nogi, Y., Nost, O. A., Popov, S. V., Rignot, E., Rippin, D. M., Rivera, A., Roberts, J., Ross, N., Siegert, M. J., Smith, A. M., Steinhage, D., Studinger, M., Sun, B., Tinto, B. K., Welch, B. C., Wilson, D., Young, D. A., Xiangbin, C., and Zirizzotti, A.: Bedmap2: Improved Ice Bed, Surface and Thickness Datasets for Antarctica, The Cryosphere, 7, 375–393, https://doi.org/10.5194/tc-7-375-2013, 2013.

Frieler, K., Clark, P. U., He, F., Buizert, C., Reese, R., Ligtenberg, S. R. M., van den Broeke, M. R., Winkelmann, R., and Levermann, A.: Consistent Evidence of Increasing Antarctic Accumulation with Warming, Nature Climate Change, 5, 348–352, https://doi.org/10.1038/nclimate2574, 2015.

Goldberg, D., Holland, D. M., and Schoof, C.: Grounding Line Movement and Ice Shelf Buttressing in Marine Ice Sheets, Journal of Geophysical Research, 114, https://doi.org/10.1029/2008JF001227, 2009.

Greve, R. and Blatter, H.: Dynamics of Ice Sheets and Glaciers, Advances in Geophysical and Environmental Mechanics and Mathematics, Springer Berlin Heidelberg, Berlin, Heidelberg, https://doi.org/10.1007/978-3-642-03415-2, 2009.

Gudmundsson, G. H., Krug, J., Durand, G., Favier, L., and Gagliardini, O.: The Stability of Grounding Lines on Retrograde Slopes, The Cryosphere, 6, 1497–1505, https://doi.org/10.5194/tc-6-1497-2012, 2012.

Haseloff, M. and Sergienko, O. V.: The Effect of Buttressing on Grounding Line Dynamics, Journal of Glaciology, 64, 417–431, https://doi.org/10.1017/jog.2018.30, 2018.

Haseloff, M., Schoof, C., and Gagliardini, O.: A Boundary Layer Model for Ice Stream Margins, Journal of Fluid Mechanics, 781, 353–387, https://doi.org/10.1017/jfm.2015.503, 2015.

Hughes, T.: Is the West Antarctic Ice Sheet Disintegrating?, Journal of Geophysical Research, 78, 7884–7910, https://doi.org/10.1029/JC078i033p07884, 1973.

Joughin, I., MacAyeal, D. R., and Tulaczyk, S.: Basal Shear Stress of the Ross Ice Streams from Control Method Inversions, Journal of Geophysical Research: Solid Earth, 109, https://doi.org/10.1029/2003JB002960, 2004.

Joughin, I., Smith, B. E., and Medley, B.: Marine Ice Sheet Collapse Potentially Under Way for the Thwaites Glacier Basin, West Antarctica, Science, 344, 735–738, https://doi.org/10.1126/science.1249055, 2014.

Joughin, I., Smith, B. E., and Howat, I. M.: A Complete Map of Greenland Ice Velocity Derived from Satellite Data Collected over 20 Years, Journal of Glaciology, 64, 1–11, https://doi.org/10.1017/jog.2017.73, 2018.

Khroulev, C. and Authors, P.: PISM, a Parallel Ice Sheet Model v1.0. Users's Manual, 2020.

Konrad, H., Shepherd, A., Gilbert, L., Hogg, A. E., McMillan, M., Muir, A., and Slater, T.: Net Retreat of Antarctic Glacier Grounding Lines, Nature Geoscience, 11, 258–262, https://doi.org/10.1038/s41561-018-0082-z, 2018.

Kundu, P., Cohen, I., and Hu, H.: Fluid Mechanics, Edition, Academic Press, New Delhi, 2012.

Leguy, G. R., Lipscomb, W. H., and Asay-Davis, X. S.: Marine Ice Sheet Experiments with the Community Ice Sheet Model, The Cryosphere, 15, 3229–3253, https://doi.org/10.5194/tc-15-3229-2021, 2021.

Levermann, A. and Feldmann, J.: Scaling of Instability Timescales of Antarctic Outlet Glaciers Based on One-Dimensional Similitude Analysis, The Cryosphere, 13, 1621–1633, https://doi.org/10.5194/tc-13-1621-2019, 2019.

Levermann, A., Winkelmann, R., Albrecht, T., Goelzer, H., Golledge, N. R., Greve, R., Huybrechts, P., Jordan, J., Leguy, G., Martin, D., Morlighem, M., Pattyn, F., Pollard, D., Quiquet, A., Rodehacke, C., Seroussi, H., Sutter, J., Zhang, T., Van Breedam, J., Calov, R., DeConto, R., Dumas, C., Garbe, J., Gudmundsson, G. H., Hoffman, M. J., Humbert, A., Kleiner, T., Lipscomb, W. H., Meinshausen, M., Ng, E., Nowicki, S. M. J., Perego, M., Price, S. F., Saito, F., Schlegel, N.-J., Sun, S., and van de Wal, R. S. W.: Projecting Antarctica's Contribution to Future Sea Level Rise from Basal Ice Shelf Melt Using Linear Response Functions of 16 Ice Sheet Models (LARMIP-2), Earth System Dynamics, 11, 35–76, https://doi.org/10.5194/esd-11-35-2020, 2020.

Lhermitte, S., Sun, S., Shuman, C., Wouters, B., Pattyn, F., Wuite, J., Berthier, E., and Nagler, T.: Damage Accelerates Ice Shelf Instability and Mass Loss in Amundsen Sea Embayment, Proceedings of the National Academy of Sciences, 117, 24 735–24 741, https://doi.org/10.1073/pnas.1912890117, 2020.

MacAyeal, D. R.: Large-Scale Ice Flow over a Viscous Basal Sediment: Theory and Application to Ice Stream B, Antarctica, Journal of Geophysical Research: Solid Earth, 94, 4071–4087, https://doi.org/10.1029/JB094iB04p04071, 1989.

Maier, N., Humphrey, N., Harper, J., and Meierbachtol, T.: Sliding Dominates Slow-Flowing Margin Regions, Greenland Ice Sheet, Science Advances, 5, eaaw5406, https://doi.org/10.1126/sciadv.aaw5406, 2019.

Mercer, J. H.: West Antarctic Ice Sheet and CO2 Greenhouse Effect: A Threat of Disaster, Nature, 271, 321–325, https://doi.org/10.1038/271321a0, 1978.

Morland, L. W.: Unconfined Ice-Shelf Flow, in: Dynamics of the West Antarctic Ice Sheet, edited by Van der Veen, C. J. and Oerlemans, J., Glaciology and Quaternary Geology, pp. 99–116, Springer Netherlands, 1987.

Morlighem, M., Seroussi, H., Larour, E., and Rignot, E.: Inversion of Basal Friction in Antarctica Using Exact and Incomplete Adjoints of a Higher-Order Model: ANTARCTIC BASAL FRICTION INVERSION, Journal of Geophysical Research: Earth Surface, 118, 1746–1753, https://doi.org/10.1002/jgrf.20125, 2013.

Morlighem, M., Rignot, E., Mouginot, J., Seroussi, H., and Larour, E.: Deeply Incised Submarine Glacial Valleys beneath the Greenland Ice Sheet, Nature Geoscience, 7, 418–422, https://doi.org/10.1038/ngeo2167, 2014.

Morlighem, M., Williams, C. N., Rignot, E., An, L., Arndt, J. E., Bamber, J. L., Catania, G., Chauché, N., Dowdeswell, J. A., Dorschel,
     B., Fenty, I., Hogan, K., Howat, I., Hubbard, A., Jakobsson, M., Jordan, T. M., Kjeldsen, K. K., Millan, R., Mayer, L., Mouginot, J.,
     Noël, B. P. Y., O'Cofaigh, C., Palmer, S., Rysgaard, S., Seroussi, H., Siegert, M. J., Slabon, P., Straneo, F., van den Broeke, M. R.,
640   Weinrebe, W., Wood, M., and Zinglersen, K. B.: BedMachine v3: Complete Bed Topography and Ocean Bathymetry Mapping of
     Greenland From Multibeam Echo Sounding Combined With Mass Conservation, Geophysical Research Letters, 44, 11,051–11,061,
     https://doi.org/10.1002/2017GL074954, 2017.

Morlighem, M., Rignot, E., Binder, T., Blankenship, D., Drews, R., Eagles, G., Eisen, O., Ferraccioli, F., Forsberg, R., Fretwell, P., Goel,
     V., Greenbaum, J. S., Gudmundsson, H., Guo, J., Helm, V., Hofstede, C., Howat, I., Humbert, A., Jokat, W., Karlsson, N. B., Lee, W. S.,
645   Matsuoka, K., Millan, R., Mouginot, J., Paden, J., Pattyn, F., Roberts, J., Rosier, S., Ruppel, A., Seroussi, H., Smith, E. C., Steinhage, D.,
     Sun, B., van den Broeke, M. R., van Ommen, T. D., van Wessem, M., and Young, D. A.: Deep Glacial Troughs and Stabilizing Ridges
     Unveiled beneath the Margins of the Antarctic Ice Sheet, Nature Geoscience, 13, 132–137, https://doi.org/10.1038/s41561-019-0510-8,
     2020.

Mouginot, J., Rignot, E., and Scheuchl, B.: Sustained Increase in Ice Discharge from the Amundsen Sea Embayment, West Antarctica, from
650   1973 to 2013, Geophysical Research Letters, 41, 1576–1584, https://doi.org/10.1002/2013GL059069, 2014.

Mouginot, J., Rignot, E., and Scheuchl, B.: Continent-Wide, Interferometric SAR Phase, Mapping of Antarctic Ice Velocity, Geophysical
     Research Letters, 46, 1–9, https://doi.org/10.1029/2019GL083826, 2019.

Nye, J. F.: The Flow of a Glacier in a Channel of Rectangular, Elliptic or Parabolic Cross-Section, Journal of Glaciology, 5, 661–690,
     https://doi.org/10.3189/S0022143000018670, 1965.

655 Pattyn, F. and Morlighem, M.: The Uncertain Future of the Antarctic Ice Sheet, Science, 367, 1331–1335,
     https://doi.org/10.1126/science.aaz5487, 2020.

Pattyn, F., Perichon, L., Durand, G., Favier, L., Gagliardini, O., Hindmarsh, R. C., Zwinger, T., Albrecht, T., Cornford, S., Docquier, D.,
     Fürst, J. J., Goldberg, D., Gudmundsson, G. H., Humbert, A., Hütten, M., Huybrechts, P., Jouvet, G., Kleiner, T., Larour, E., Martin,
     D., Morlighem, M., Payne, A. J., Pollard, D., Rückamp, M., Rybak, O., Seroussi, H., Thoma, M., and Wilkens, N.: Grounding-Line
660   Migration in Plan-View Marine Ice-Sheet Models: Results of the Ice2sea MISMIP3d Intercomparison, Journal of Glaciology, 59, 410–
     422, https://doi.org/10.3189/2013JoG12J129, 2013.

Pegler, S. S.: Suppression of Marine Ice Sheet Instability, Journal of Fluid Mechanics, 857, 648–680, https://doi.org/10.1017/jfm.2018.742,
     2018.

Pegler, S. S., Kowal, K. N., Hasenclever, L. Q., and Worster, M. G.: Lateral Controls on Grounding-Line Dynamics, Journal of Fluid
665   Mechanics, 722, https://doi.org/10.1017/jfm.2013.140, 2013.

Pritchard, H. D., Arthern, R. J., Vaughan, D. G., and Edwards, L. A.: Extensive Dynamic Thinning on the Margins of the Greenland and
     Antarctic Ice Sheets, Nature, 461, 971–975, https://doi.org/10.1038/nature08471, 2009.

Rayleigh: The Principle of Similitude, Nature, 95, 66–68, https://doi.org/10.1038/095066c0, 1915.

Raymond, C.: Shear Margins in Glaciers and Ice Sheets, Journal of Glaciology, 42, 90–102, https://doi.org/10.3189/S0022143000030550,
670   1996.

Reynolds, O.: An Experimental Investigation of the Circumstances Which Determine Whether the Motion of Water Shall Be Direct or
     Sinuous, and of the Law of Resistance in Parallel Channels, Philosophical Transactions of the Royal Society of London, 174, 935–982,
     https://doi.org/10.1098/rstl.1883.0029, 1883.

Rignot, E. and Mouginot, J.: Ice Flow in Greenland for the International Polar Year 2008–2009, Geophysical Research Letters, 39, https://doi.org/10.1029/2012GL051634, 2012.

Rignot, E., Mouginot, J., Morlighem, M., Seroussi, H., and Scheuchl, B.: Widespread, Rapid Grounding Line Retreat of Pine Island, Thwaites, Smith, and Kohler Glaciers, West Antarctica, from 1992 to 2011, Geophysical Research Letters, 41, 3502–3509, https://doi.org/10.1002/2014GL060140, 2014.

Rignot, E., Mouginot, J., Scheuchl, B., van den Broeke, M., van Wessem, M. J., and Morlighem, M.: Four Decades of Antarctic Ice Sheet Mass Balance from 1979–2017, Proceedings of the National Academy of Sciences, 116, 1095–1103, https://doi.org/10.1073/pnas.1812883116, 2019.

Schoof, C.: Ice Sheet Grounding Line Dynamics: Steady States, Stability, and Hysteresis, Journal of Geophysical Research, 112, https://doi.org/10.1029/2006JF000664, 2007.

Schoof, C., Davis, A. D., and Popa, T. V.: Boundary Layer Models for Calving Marine Outlet Glaciers, The Cryosphere, 11, 2283–2303, https://doi.org/10.5194/tc-11-2283-2017, 2017.

Sergienko, O. V. and Hindmarsh, R. C. A.: Regular Patterns in Frictional Resistance of Ice-Stream Beds Seen by Surface Data Inversion, Science, 342, 1086–1089, https://doi.org/10.1126/science.1243903, 2013.

Sergienko, O. V. and Wingham, D. J.: Grounding Line Stability in a Regime of Low Driving and Basal Stresses, Journal of Glaciology, 65, 833–849, https://doi.org/10.1017/jog.2019.53, 2019.

Sergienko, O. V., Creyts, T. T., and Hindmarsh, R. C. A.: Similarity of Organized Patterns in Driving and Basal Stresses of Antarctic and Greenland Ice Sheets beneath Extensive Areas of Basal Sliding, Geophysical Research Letters, 41, 3925–3932, https://doi.org/10.1002/2014GL059976, 2014.

Seroussi, H. and Morlighem, M.: Representation of Basal Melting at the Grounding Line in Ice Flow Models, The Cryosphere, 12, 3085–3096, https://doi.org/10.5194/tc-12-3085-2018, 2018.

Seroussi, H., Nakayama, Y., Larour, E., Menemenlis, D., Morlighem, M., Rignot, E., and Khazendar, A.: Continued Retreat of Thwaites Glacier, West Antarctica, Controlled by Bed Topography and Ocean Circulation: ICE-OCEAN MODELING OF THWAITES GLACIER, Geophysical Research Letters, 44, 6191–6199, https://doi.org/10.1002/2017GL072910, 2017.

Seroussi, H., Nowicki, S., Payne, A. J., Goelzer, H., Lipscomb, W. H., Abe-Ouchi, A., Agosta, C., Albrecht, T., Asay-Davis, X., Barthel, A., Calov, R., Cullather, R., Dumas, C., Galton-Fenzi, B. K., Gladstone, R., Golledge, N. R., Gregory, J. M., Greve, R., Hattermann, T., Hoffman, M. J., Humbert, A., Huybrechts, P., Jourdain, N. C., Kleiner, T., Larour, E., Leguy, G. R., Lowry, D. P., Little, C. M., Morlighem, M., Pattyn, F., Pelle, T., Price, S. F., Quiquet, A., Reese, R., Schlegel, N.-J., Shepherd, A., Simon, E., Smith, R. S., Straneo, F., Sun, S., Trusel, L. D., Van Breedam, J., van de Wal, R. S. W., Winkelmann, R., Zhao, C., Zhang, T., and Zwinger, T.: ISMIP6 Antarctica: A Multi-Model Ensemble of the Antarctic Ice Sheet Evolution over the 21st Century, The Cryosphere, 14, 3033–3070, https://doi.org/10.5194/tc-14-3033-2020, 2020.

Shepherd, A., Gilbert, L., Muir, A. S., Konrad, H., McMillan, M., Slater, T., Briggs, K. H., Sundal, A. V., Hogg, A. E., and Engdahl, M. E.: Trends in Antarctic Ice Sheet Elevation and Mass, Geophysical Research Letters, 0, https://doi.org/10.1029/2019GL082182, 2019.

Szücs, E.: Fundamental Studies in Engineering II, Similitude and Modeling, Elsevier Scientific Publishing Co., Amsterdam, Netherlands, 1980.

The IMBIE team: Mass Balance of the Antarctic Ice Sheet from 1992 to 2017, Nature, 558, 219–222, https://doi.org/10.1038/s41586-018-0179-y, 2018.

The IMBIE Team: Mass Balance of the Greenland Ice Sheet from 1992 to 2018, Nature, 579, 233–239, https://doi.org/10.1038/s41586-019-1855-2, 2020.

Weertman, J.: Stability of the Junction of an Ice Sheet and an Ice Shelf, Journal of Glaciology, 13, 3–11, https://doi.org/10.3189/S0022143000023327, 1974.

715   Wessem, J. M. V., Reijmer, C. H., Morlighem, M., Mouginot, J., Rignot, E., Medley, B., Joughin, I., Wouters, B., Depoorter, M. A., Bamber, J. L., Lenaerts, J. T. M., Berg, W. J. V. D., Broeke, M. R. V. D., and Meijgaard, E. V.: Improved Representation of East Antarctic Surface Mass Balance in a Regional Atmospheric Climate Model, Journal of Glaciology, 60, 761–770, https://doi.org/10.3189/2014JoG14J051, 2014.

Winkelmann, R., Martin, M. A., Haseloff, M., Albrecht, T., Bueler, E., Khroulev, C., and Levermann, A.: The Potsdam Parallel Ice Sheet
720   Model (PISM-PIK) – Part 1: Model Description, The Cryosphere, 5, 715–726, https://doi.org/10.5194/tc-5-715-2011, 2011.

Zhang, T., Price, S. F., Hoffman, M. J., Perego, M., and Asay-Davis, X.: Diagnosing the Sensitivity of Grounding-Line Flux to Changes in Sub-Ice-Shelf Melting, The Cryosphere, 14, 3407–3424, https://doi.org/10.5194/tc-14-3407-2020, 2020.
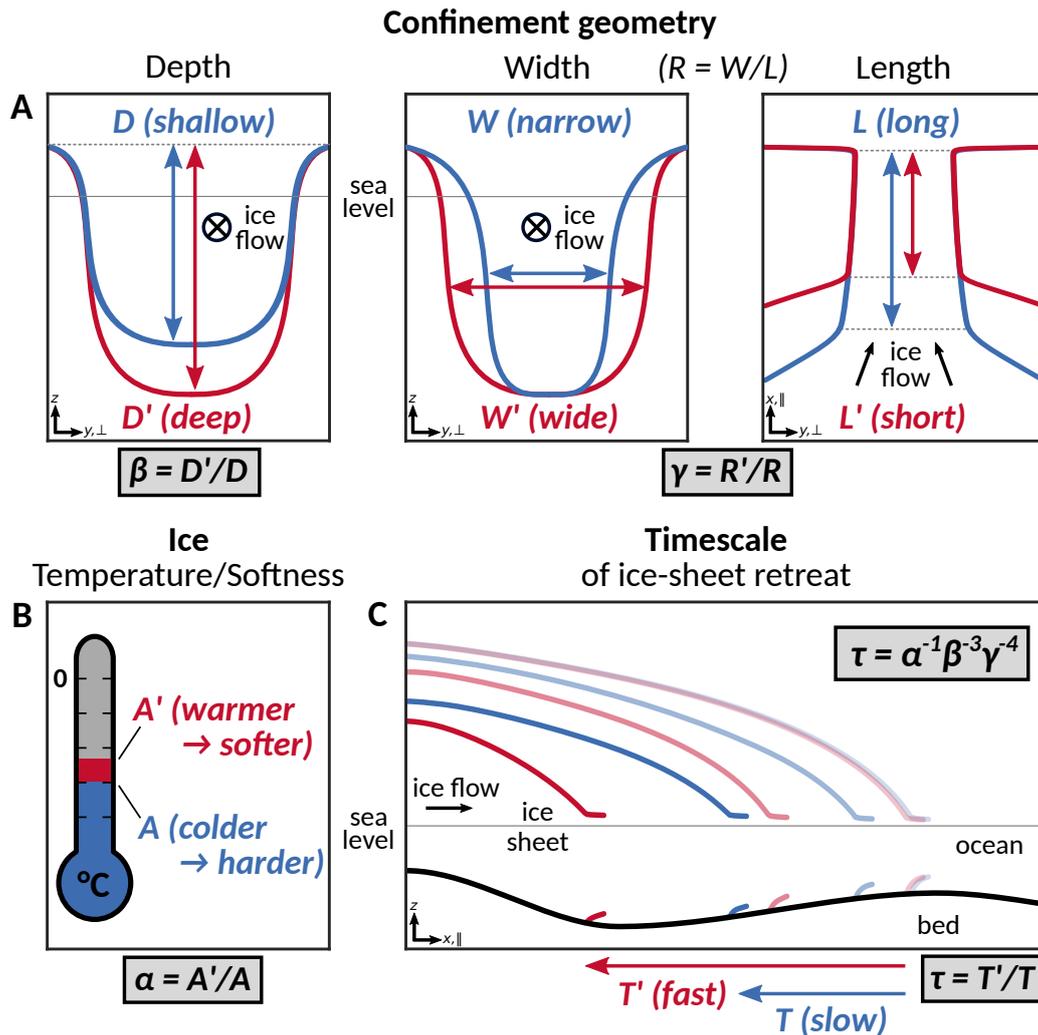
Figure 1. Schematic showing the influence of (**A**) the geometry (depth, width, length scales) of the confinement of fast ice flow, and (**B**) the temperature-dependent ice softness on (**C**) the timescale of ice-sheet retreat. The involved scaling variables and the scaling relation resulting from similitude analysis (Eq. 4) are given in grey boxes. The main flow direction is along the trough, denoted by the ‖ symbol, as used in Eq. (1). Note that the application of the scaling relation to the timescale of ice-sheet retreat is based on the assumption that the flow velocity itself and its spatial derivative are proportional. For simplicity this schematic shows the case of a strongly topographically controlled ice-stream confinement.
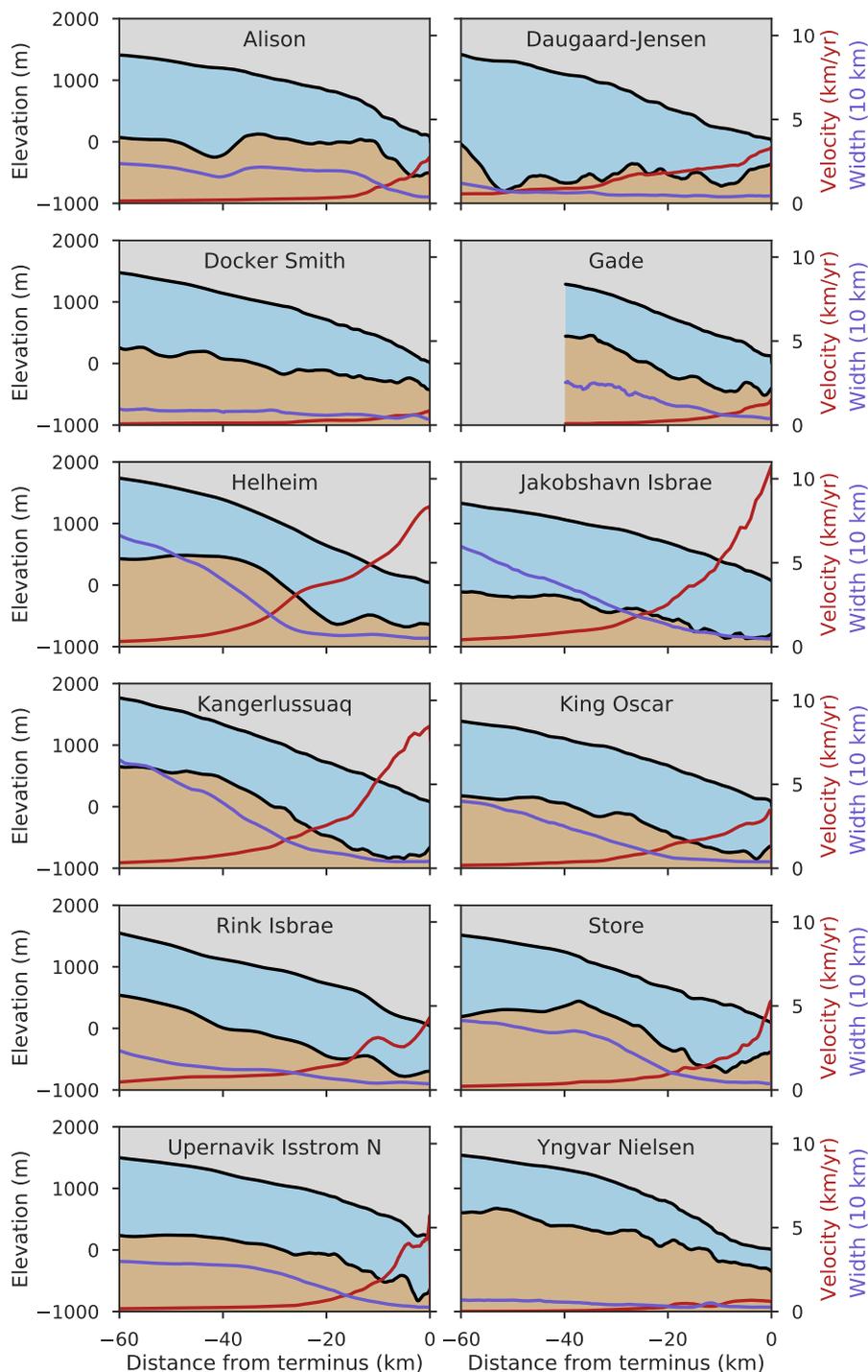
Figure 2. Profiles for twelve different glacier outlets across Greenland obtained from Beckmann et al. (2019), based on observational data. Bed topography in brown, glacier ice in blue. Ice speed and confinement width in red and purple, respectively ($y-$axis on right-hand-side).
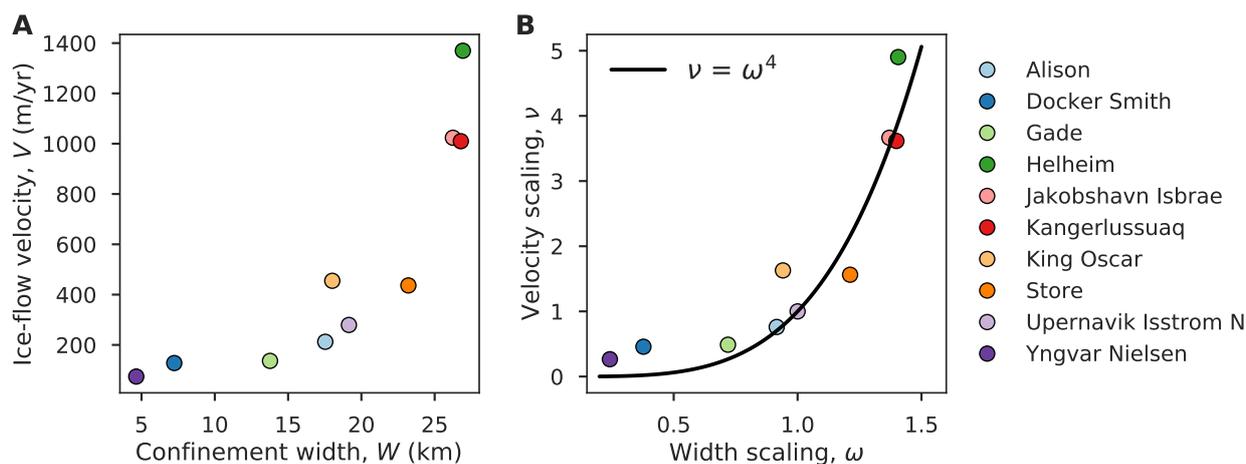
Figure 3. Scaling of observed ice-flow speed of Greenland outlet glaciers dependent on their width. **(A)** Ice-flow velocity inside the confinement versus confinement width extracted from observations. **(B)** Data normed to reference glacier Upernavik Isstrom N (light purple). The black curve shows the quartic relation between the scaling of the velocity, ν, and the glacier width, ω, as predicted by the scaling law (Eq. 4). Please note that there is no fudge factor between observation and theory in panel **B**. Glacier names are given in the legend.
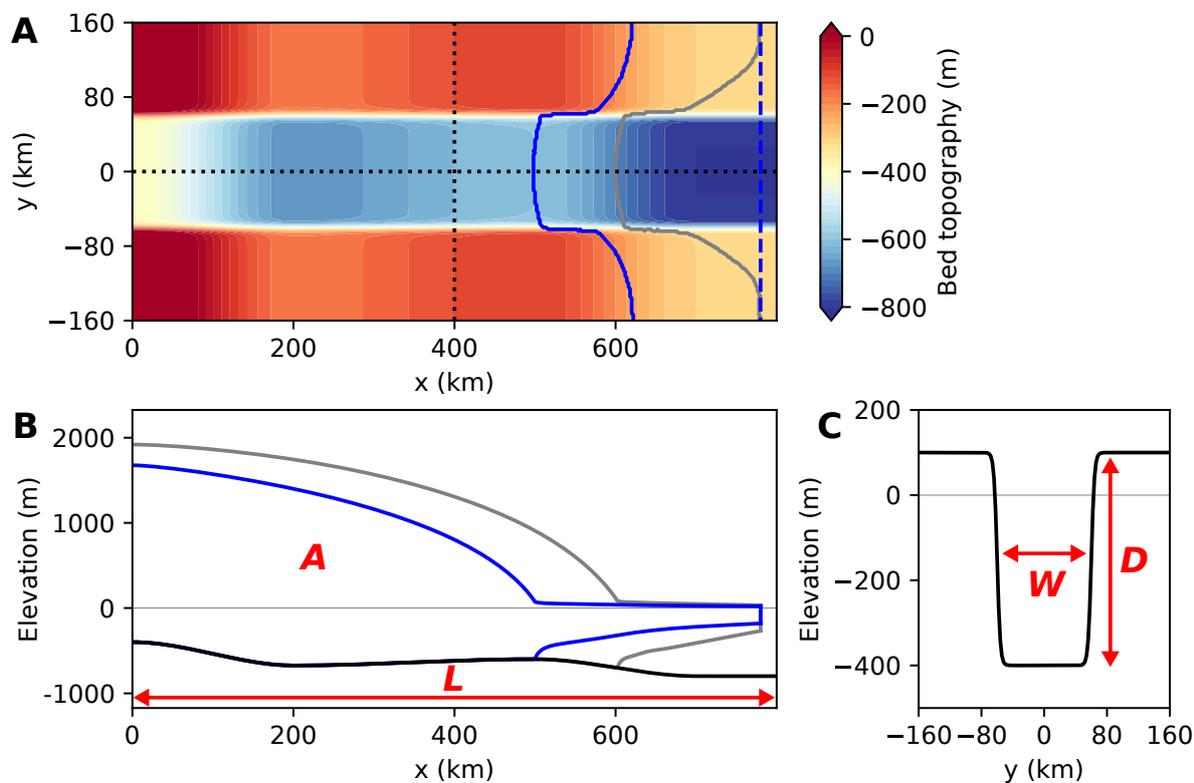
Figure 4. (A) Bed topography applied in the simulations (colorbar) with contours of the grounding line after $1,000$ model years (grey) and after equilibration (blue) for a stable configuration (bed-trough width $W = 100$ km). Fixed calving-front position shown by dashed line. Dotted lines denote cross sections **(B)** along the centerline of the setup ($y = 0$) and **(C)** across the bed trough ($x = 400$ km). The profiles of the ice-sheet-shelf system are shown in colors corresponding to panel **(A)**. The bed topography is shown in black. The length scale L, the width W and the depth D of the confinement, and the ice softness A, which are the parameters varied throughout the experiments, are highlighted in red.
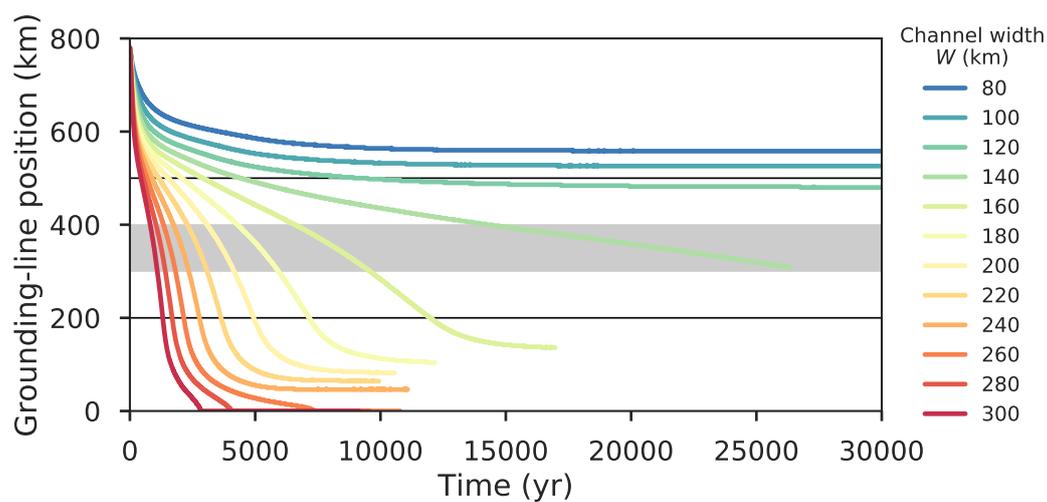
Figure 5. Evolution of the centerline grounding-line position (along $y = 0$) of the simulated ice-sheet-shelf system from in initialization to equilibration, here exemplarly shown for a variation of the channel width W. Horizontal black lines denote endpoints of the retrograde section of the bed topography (see Fig. 4B). The characteristic timescale is obtained by averaging the retreat time over the central 100-km long retrograde bed section (grey-shaded region).
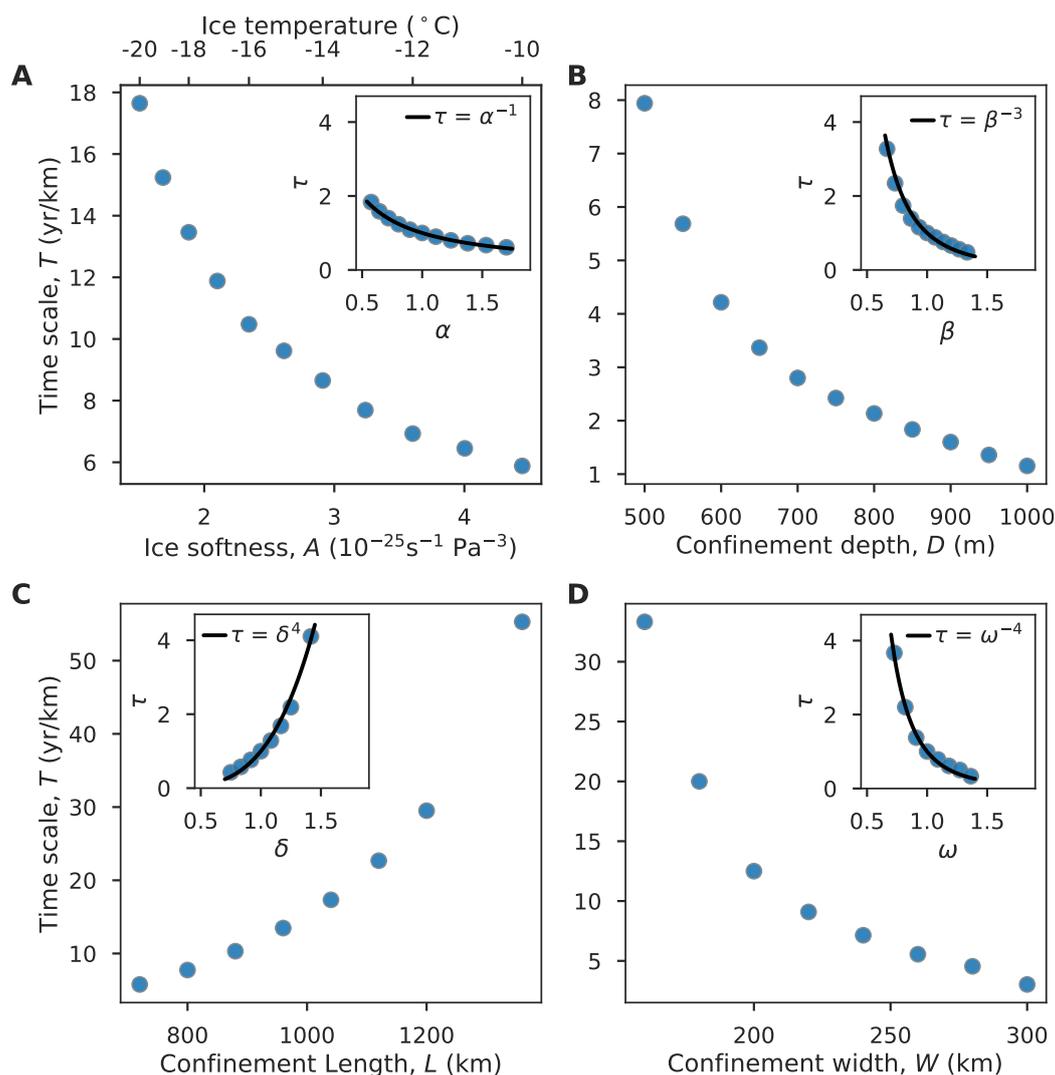
Figure 6. Time scaling of simulated unstable ice-sheet retreat. Characteristic retreat timescale T down the retrograde bed slope (measured in years per km of retreat) dependent on **(A)** the ice softness A, **(B)** the depth of the confinement D, **(C)** the length scale of the confinement L and **(D)** the width of the confinement W. The insets show the scaling if data is normed to a reference softness / confinement depth / confinement length scale / confinement width and the associated reference timescale. The black curves give the scaling behavior according to the analytically-derived scaling relation (Eq. 4). Please note that there is no fudge factor between simulations and theory.
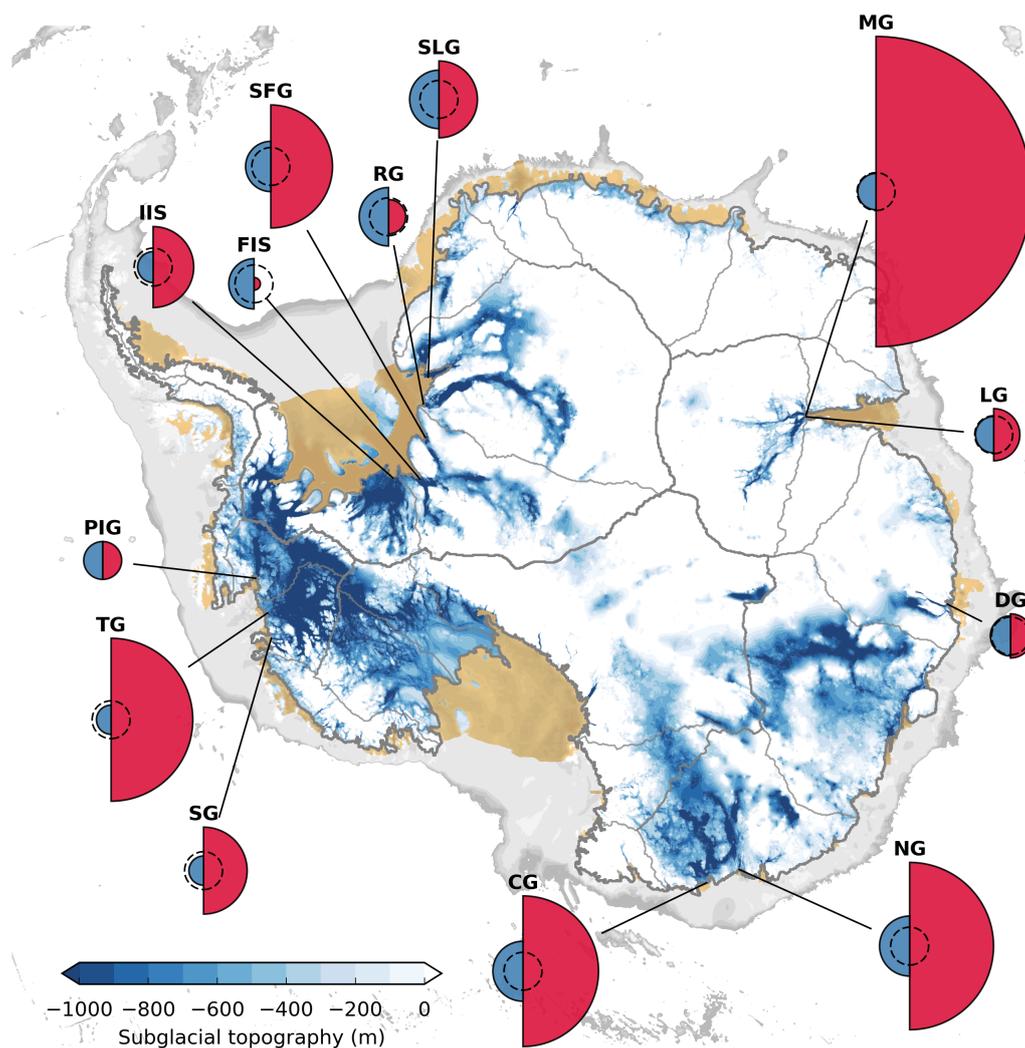
Figure 7. Inverse timescales of MISI-prone Antarctic outlet glaciers and their sea-level potential. Areas of red semi circles represent median values of the initial retreat speed after a potential destabilization ($<\tau>^{-1}$). Areas of blue semi circles correspond to the sea-level equivalent of the ice in the marine portions of the drainage basin(s) of the respective outlets. All values are calculated relative to the reference system Pine Island Glacier (PIG, dashed circles). Timescale values and abbreviations of the outlet names are given in Table 3.
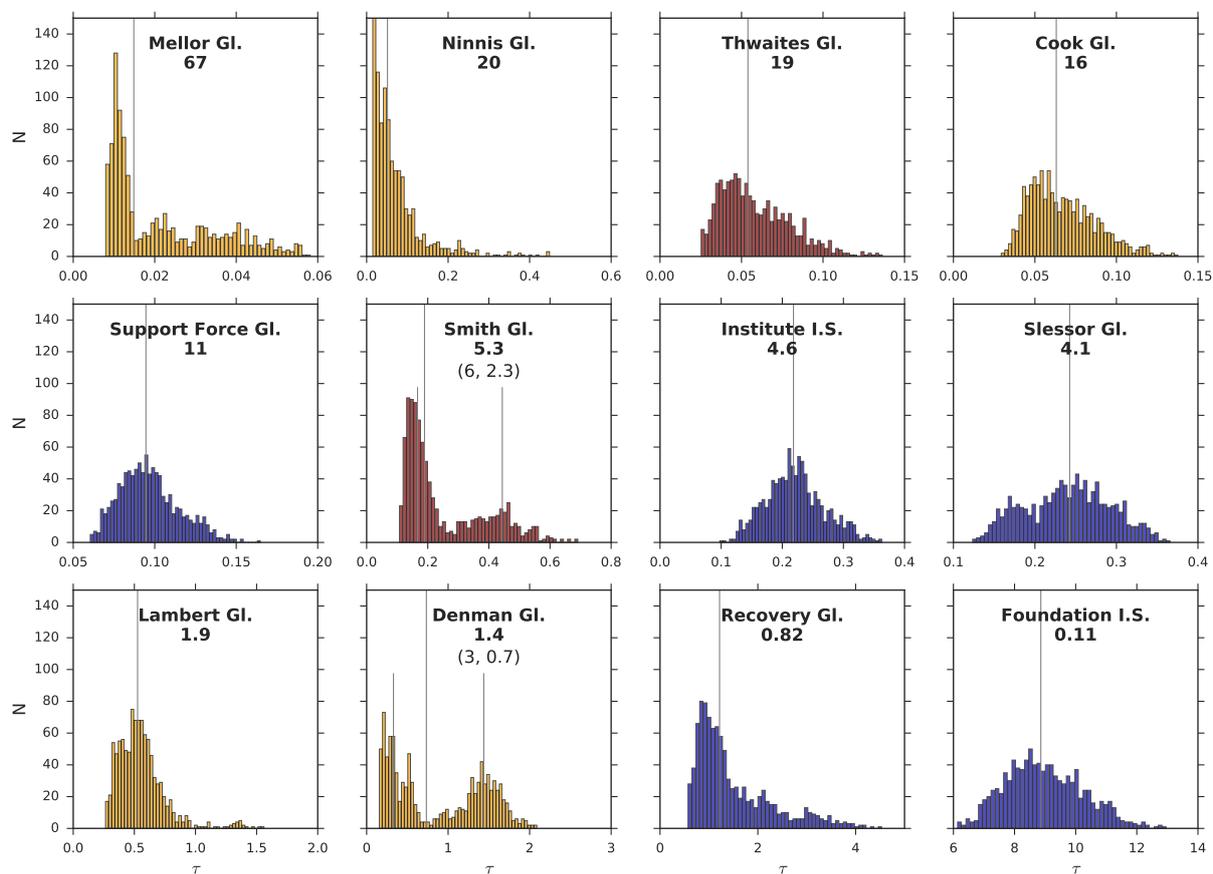
Figure 8. Probability distributions of the retreat-timescale ratios. Median values $\langle\tau\rangle$ are shown by vertical lines. The values given below the glacier names are the inverse of the median ($\langle\tau\rangle^{-1}$), i.e., the retreat-speed ratios. Locations of the outlets: Amundsen Sea Sector (red), East Antarctica (yellow) and Filchner-Ronne Ice Shelf (blue).

Table 1. Definition of scales and their ratios.

Category	Scaling ratio	Letter	Definition
Thermodynamics	Softness	α	A'/A
Geometry	Depth	β	D'/D
	Length	δ	L'/L
	Width	ω	W'/W
	Depth gradient	Γ	$\beta/\delta = (D'/L')/(D/L)$
	Horizontal aspect ratio	γ	$\omega/\delta = R'/R = (W'/L')/(W/L)$
Kinematics	Time	τ	T'/T
	Velocity	ν	$\delta/\tau = V'/V = (L'/T')/(L/T)$
	Volume flux	μ	$\nu\,\beta\,\omega = (V'\,D'\,W')/(V\,D\,W)$

Table 2. Physical constants and parameter values as prescribed in the simulations.

Parameter	Value	Unit	Physical meaning
a	0.15	m yr^{-1}	Surface mass balance
A_0	$3.615 \cdot 10^{-13}$	Pa^{-3} s^{-1}	Pre-exponential factor in Eq. (C1)
C	$3.981 \cdot 10^6$	Pa m$^{-1/3}$ s$^{1/3}$	Basal friction parameter in Eq. (C2)
g	9.81	m s^{-2}	Gravitational acceleration
m	1/3		Basal friction exponent in Eq. (C2)
n	3		Exponent in Glen's law
s	$2.5 \cdot 10^{-4}$		Reference mean slope magnitude of retrograde bed section
Q	$6 \cdot 10^4$	J mol^{-1}	Activation energy in Eq. (C1)
R_g	8.314	J K^{-1} mol^{-1}	Universal gas constant in Eq. (C1)
T_{ice}	$\{-20, -19, ..., -11, -10\}$	°C	Ice temperature entering Eq. (C1)
d_c	$\{500, 550, ..., 950, 1000\}$	m	Depth of bed trough compared with side walls, entering Eq. (1) of Cornford et al. (2020)
f_c	4	km	Characteristic width of bed-trough side walls, entering Eq. (1) of Cornford et al. (2020)
l_c	$\{720, 800, ..., 1280, 1360\}$	km	Length of bed trough
w_c	$\{40, 50, ..., 140, 150\}$	km	Half-width of bed trough, entering Eq. (1) of Cornford et al. (2020)
x_{cf}	$0.975 \cdot l_c$	km	Position of fixed calving front
ρ	918	kg m^{-3}	Ice density

Table 3. Median values of inferred scaling-ratio distributions for ice softness $<\alpha>$, confinement depth $<\beta>$, confinement length $<\delta>$, confinement width $<\omega>$ and time $<\tau>$. Last column gives the likely range of τ (17th - 83rd percentile).

Outlet glacier	$<\alpha>$	$<\beta>$	$<\delta>$	$<\omega>$	$<\tau>$	$\Delta\tau$
Amundsen Sea Sector						
Pine Island Glacier (PIG)	1.0	1.0	1.0	1.0	1.0	-
Thwaites Glacier (TG)	0.77	0.63	0.58	2.08	0.054	0.025 - 0.137
Smith Glacier (SG)	1.13	0.91	0.29	0.53	0.189	0.107 - 0.692
East Antarctica						
Cook Glacier (CG)	0.76	0.53	1.11	3.76	0.063	0.029 - 0.138
Ninnis Glacier (NG)	0.42	1.04	0.43	1.05	0.051	0.014 - 0.449
Denman Glacier (DG)	0.56	0.81	0.28	0.45	0.733	0.153 - 2.091
Lambert Glacier (LG)	0.48	0.82	0.55	0.9	0.526	0.262 - 1.562
Mellor Glacier (MG)	0.48	1.8	0.18	0.45	0.015	0.008 - 0.058
Filchner-Ronne Ice Shelf						
Slessor Glacier (SLG)	0.65	0.86	1.27	2.18	0.243	0.123 - 0.366
Recovery Glacier (RG)	0.54	1.2	1.05	0.9	1.217	0.576 - 4.537
Support Force Glacier (SFG)	0.62	1.12	0.49	0.98	0.095	0.060 - 0.165
Foundation Ice Stream (FIS)	0.45	1.81	2.46	1.13	8.861	6.127 - 12.968
Institute Ice Stream (IIS)	0.6	0.94	1.55	2.26	0.218	0.097 - 0.363